

## Mid-infrared optical constants of clinopyroxene and orthoclase derived from oriented single-crystal reflectance spectra

JESSICA A. ARNOLD<sup>1,\*</sup>, TIMOTHY D. GLOTCH<sup>1</sup> AND ANNA M. PLONKA<sup>1</sup>

<sup>1</sup>Department of Geosciences, Stony Brook University, Stony Brook, New York 11794, U.S.A.

### ABSTRACT

We have determined the mid-IR optical constants of one alkali feldspar and four pyroxene compositions in the range of 250–4000  $\text{cm}^{-1}$ . Measured reflectance spectra of oriented single crystals were iteratively fit to modeled spectra derived from classical dispersion analysis. We present the real and imaginary indices of refraction ( $n$  and  $k$ ) along with the oscillator parameters with which they were modeled. While materials of orthorhombic symmetry and higher are well covered by the current literature, optical constants have been derived for only a handful of geologically relevant monoclinic materials, including gypsum and orthoclase. Two input parameters that go into radiative transfer models, the scattering phase function and the single scattering albedo, are functions of a material's optical constants. Pyroxene is a common rock-forming mineral group in terrestrial bodies as well as meteorites and is also detected in cosmic dust. Hence, having a set of pyroxene optical constants will provide additional details about the composition of Solar System bodies and circumstellar materials. We follow the method of Mayerhöfer et al. (2010), which is based on the Berreman  $4 \times 4$  matrix formulation. This approach provides a consistent way to calculate the reflectance coefficients in low-symmetry cases. Additionally, while many models assume normal incidence to simplify the dispersion relations, this more general model applies to reflectance spectra collected at non-normal incidence.

**Keywords:** Spectroscopy, infrared measurements, planetary surfaces, mineralogy

### INTRODUCTION

Pyroxenes are common rock-forming minerals in terrestrial planets and asteroids. They are also abundant in meteorites and interplanetary and cosmic dust particles. The pyroxene crystal structure allows for various cations to occupy its M1 and M2 sites, with ordering and preference between the two sites being controlled by temperature, pressure, and cooling rate. As a result, pyroxene composition is a good indicator of the thermal history of the source magma (Klima et al. 2008) and can be used to compare the evolution of different planetary bodies (Karner et al. 2006). Pyroxene is readily detected in the near-infrared (NIR) via two strong  $\text{Fe}^{2+}$  crystal field absorption bands near 1 and 2  $\mu\text{m}$  whose positions and strengths are functions of composition. As the mid-IR (MIR, around 3–15  $\mu\text{m}$ , although definitions vary) is sensitive to Si-O vibrational modes (Salisbury 1972), it can be used to provide additional details about composition as well as to estimate abundance relative to more felsic components (Ramsey and Christensen 1998).

The wavelength-dependent complex index of refraction ( $\tilde{n} = n + ik$ ), where  $n$  and  $k$  are the optical constants, is an essential input into scattering models of planetary surfaces. Commonly used radiative transfer models of airless bodies include Lumme and Howell (1981), Hapke (1993, 2012), Shkuratov et al. (1999), and Mishchenko et al. (1999). Hapke's theory uses optical constants to calculate the single scattering albedo and the phase function. In Shkuratov's model of lunar regolith scattering, the reflectance of the surface ( $A$ ) depends on only four parameters  $A(n, k, S, q)$ , where  $n$  and  $k$  are the optical constants,  $S$  is the scattering path-length, and  $q$  is the packing density (Shkuratov et

al. 1999). Hence, accurate determination of optical constants for various minerals is necessary for using remote sensing data to make quantitative estimates of mineralogical composition. At MIR wavelengths, materials of orthorhombic symmetry and higher are well covered by the current literature; these include quartz, calcite, olivine, orthopyroxene, kaolinite, serpentine, palagonite, and iron oxides (Spitzer and Kleinman 1961; Wenrich and Christensen 1996; Lucy 1998; Lane 1999; Suto et al. 2002; Glotch et al. 2006; Sogawa et al. 2006; Dyar et al. 2009; Roush et al. 1991; Glotch and Rossman 2009).

Monoclinic and triclinic minerals have largely been ignored in optical constant research, although in some cases orientation-averaged effective optical constants have been calculated and presented (e.g., Roush et al. 1991; Glotch et al. 2007). This is due to the additional complexity of obtaining values for low-symmetry materials, despite the fact that these crystal systems contain important rock-forming mineral groups such as clinopyroxene and feldspar. In this work, we use dispersion analysis to calculate the optical constants of four distinct clinopyroxene compositions in the range of 250–4000  $\text{cm}^{-1}$ , following the method of Mayerhöfer et al. (2010) and present a procedure that can be applied to derive the optical constants of monoclinic single crystals. We also calculate the optical constants of orthoclase and compare to the previously computed optical constants of Aronson (1986) as a test of our model.

### BACKGROUND

#### The Moon

The Clementine mission provided a global lunar map of pyroxene abundance, broadly highlighting that it is a major component of the mare basalts and less prevalent in highlands. Modeled

\* E-mail: jessica.a.arnold@stonybrook.edu

clinopyroxene concentrations are especially high in fresh mare craters due to the short exposure ages of these surfaces (Shkuratov et al. 2004). While pyroxene is only a minor component in the lunar highlands it is found in the following highlands rock types: ferroan anorthosites (FAN's), alkali- and Mg-suite rocks (Tompkins and Pieters 1999). Attempting to put these in a global context, Klima et al. (2011a) used NIR data from the Moon Mineralogy Mapper ( $M^3$ ) to detail the distribution of high- vs. low-Ca pyroxene and estimate Mg#. Low-Ca pyroxene is limited to regional exposures within the South Pole-Aitken Basin and in the highlands north and south of Mare Frigoris, approximately half of which have Mg# [Mg/(Mg+Fe)] commensurate with FAN rocks (~Mg# 55–75).

MIR emission data from the Diviner Lunar Radiometer Experiment complements visible near-IR (VNIR) measurements from Clementine and  $M^3$ , as they are able to detect Fe-poor lithologies in the presence of mafic materials such as pyroxene and olivine. Three of Diviner's channels are centered near the silicate Christiansen feature (CF) (Paige et al. 2010), which is an emissivity maximum whose position moves to shorter wavelengths with increasing  $SiO_2$  polymerization (Conel 1969; Logan et al. 1973; Salisbury and Walter 1989), allowing Diviner to be used to map silicate compositions across the Moon (Greenhagen et al. 2010; Glotch et al. 2010, 2011; Song et al. 2013; Allen et al. 2011; Arnold et al. 2013). A global map of CF position clearly demonstrates the difference between the relatively pyroxene-rich mare and feldspar-rich highlands (Greenhagen et al. 2010). Although Diviner has only three spectral bands in the 8  $\mu m$  range, laboratory measurements in a simulated lunar environment show the estimated CF position combined with spectral shape is adequate to distinguish pyroxene from a mixture of plagioclase and olivine (Donaldson Hanna et al. 2012).

## Mars

The low-albedo regions of Mars were initially categorized into two surface compositions based on Mars Global Surveyor Thermal Emission Spectrometer (MGS-TES) data, where Surface Type 1 was determined to be basalt containing ~25% clinopyroxene (Bandfield et al. 2000; Hamilton et al. 2001). Rogers et al. (2007) defined four distinct spectral types within low-albedo terrains. Subsequently, Rogers and Christensen (2007) determined the mineralogy of these four groups, with clinopyroxene abundance being one of the major distinguishing features. While low-Ca pyroxenes were mostly detected in Noachian terrain, high-Ca pyroxene was found in a wider age-range of units. Some of the mineralogical differences between the four groups, especially high silica phases, are the result of weathering. However, the differences in pyroxene abundance likely represent differences in the magma from which the crust was derived. These differences were also identified with data from the Observatoire pour la Minéralogie, l'Eau, les Glaces et l'Activité (OMEGA) NIR imaging spectrometer. Using this instrument, Ody et al. (2012) presented global maps of anhydrous minerals, including pyroxene. The highest pyroxene concentration occurs in the Syrtis Major volcanic province, which is coincident with Group 2 of Rogers and Christensen (2007). Glotch and Rogers (2013) suggested that the unusually high concentration of high-Ca pyroxene at this site was the result of subsurface interactions of basaltic magma and a Ca-carbonate-bearing layer.

## Asteroids

Pyroxene has been identified in several S-type asteroid families (Chapman et al. 1975). Sunshine et al. (2004) applied the Modified Gaussian Model (MGM) to VNIR asteroid spectra collected by the NASA Infrared Telescope Facility (IRTF), to determine the relative amounts of low- and high-calcium pyroxene. They determined that the Vestoids and well as the S-type asteroid families Merxia and Agnia have a high ratio of high-calcium pyroxene to total pyroxene, indicating that they are derived from differentiated bodies.

Pyroxene absorptions are the most common VNIR spectral feature on the surface of the asteroid Vesta, which was first linked to the howardite-eucrite-diogenite (HED) meteorites due to the similarity of their 0.9  $\mu m$  band in VNIR spectra (McCord et al. 1970). The findings of Dawn's visible infrared (VIR) mapping spectrometer support this connection. Much of the surface shows a howardite-like spectrum intermixed with smaller-scale regions resembling eucrites and diogenites. The south polar region (Rheasilvia), a large impact basin, is consistent with more Mg-rich pyroxene characteristic of diogenites (De Sanctis et al. 2012). These spectral variations are indicative of a differentiated crust where the deeper diogenitic materials have been exposed through impact.

## Interplanetary and interstellar dust

The presence of crystalline silicates in interplanetary dust particles (IDPs) was established through micrometeorite samples collected from Earth's stratosphere (Bradley et al. 1983; Mackinnon and Rietmeijer 1987). Additionally, ground-based MIR spectra from three different instruments provided evidence for crystalline silicates in comets (Hanner et al. 1994). Prior to the Infrared Space Observatory (ISO), whose instruments covered a range of ~2.5–240  $\mu m$ , silicates in cosmic dust were thought to be primarily amorphous (Roush et al. 1991; Molster and Kemper 2004). This assumption guided most previous laboratory studies of pyroxene optical constants (Jäger et al. 1994; Dorschner et al. 1995; Henning and Mutschke 1997). Using ISO, crystalline pyroxene was detected in dust produced by evolved stars (Molster et al. 2002), the circumstellar disks of young stellar objects (YSO's) (Bouwman et al. 2001), and planetary nebula (Beintema 1997). As a result of the detection of crystalline pyroxene around planetary nebula, Jäger et al. (1998) estimated the MIR optical constants for a natural enstatite (low-Ca orthopyroxene) sample along the crystallographic axes using Kramers-Kronig analysis. Better characterization of the materials in circumstellar environments will improve our understanding of dust formation and processing and enable comparison to our own Solar System.

## METHOD

### Sample description and preparation

All samples are large single crystals (roughly 0.5–1 cm on a side) and their chemical compositions are summarized in Table 1. The major element abundances were determined by scanning electron microscope energy-dispersive X-ray spectroscopy (SEM-EDS). To produce the chemical formulas in Table 1, atomic abundances of oxygen were assumed by stoichiometry to be  $O_6$ , which may introduce error if any non-pyroxene phases are present in the samples. We prepared thin sections of each sample to optically examine the samples for exsolution and twinning. One augite (Aug1) sample was loaned from the Stony Brook Geosciences Department mineral collection and originates from Indian Well, Arizona.

**TABLE 1.** Information for pyroxenes and orthoclase included in this study

Sample	Source (location)	Chemical formula
augite (Aug1)	SBU (Indian Well, AZ)	$\text{Na}_{0.11}\text{K}_{0.10}\text{Mg}_{0.54}\text{Fe}_{0.46}\text{Ti}_{0.13}\text{Ca}_{0.46}\text{Al}_{0.48}\text{Si}_{1.79}\text{O}_6$
diopside (Diop1)	Kelly's Rocks (Magog, QC)	$\text{Na}_{0.04}\text{Mg}_{0.64}\text{Fe}_{0.18}\text{Mn}_{0.01}\text{Ca}_{0.92}\text{Al}_{0.03}\text{Si}_{2.09}\text{O}_6$
clinopyroxene (Aug2)	SBU	$\text{Na}_{0.02}\text{Mg}_{0.57}\text{Fe}_{0.40}\text{Ti}_{0.02}\text{Ca}_{0.69}\text{Al}_{0.13}\text{Si}_{2.06}\text{O}_6$
hedenbergite (Hed1)	SBU	$\text{Na}_{0.03}\text{Mg}_{0.29}\text{Fe}_{0.51}\text{Mn}_{0.07}\text{Ca}_{0.83}\text{Al}_{0.08}\text{Si}_{2.08}\text{O}_6$
orthoclase	GGGems (Itrongay, Madagascar)	$\text{K}_{0.96}\text{Na}_{0.04}\text{Al}_{0.96}\text{Fe}_{0.04}\text{Si}_3\text{O}_8$

This sample does not show signs of exsolution or twinning. The diopside (Diop1) sample was purchased from Kelly's Rocks and is from Magog, Quebec, Canada. While twinning is present over ~30–40% of a section perpendicular to the *a-c* plane in the diopside sample, the IR spectra match previously published oriented reflectance spectra (Johnson et al. 2002). The hedenbergite (Hed1) and second augite (Aug2) sample were provided by D. Linsley at Stony Brook University. The hedenbergite sample does not exhibit exsolution or twinning, while Aug2 appears to contain lamellae that remain dark under crossed polar illumination at all orientations. Micro-FTIR spectra of these lamellae are quite noisy compared to the rest of the augite sample, and show a broad reflectance peak at around 3900  $\text{cm}^{-1}$  and a peak at 1015  $\text{cm}^{-1}$ . These spectral features indicate some type of clay, however the exact composition is difficult to discern. FTIR spectrum of the whole sample does not show a 3900  $\text{cm}^{-1}$  peak, indicating this is a relatively minor component. The diopside, hedenbergite, and augite compositions are shown on the ternary diagram in Figure 1. We cut each sample with a diamond saw blade so that one surface is parallel to the *a-c* plane (010) and the other perpendicular to it—planes (001) or (100). We polished these surfaces to 0.25  $\mu\text{m}$  surface roughness, and confirmed the orientations of the cut surfaces by single-crystal XRD. XRD analysis involved collection of the preliminary set of frames (pre-experiment) for the determination of unit cell and the orientation matrix. Using this information, we indexed the faces of the crystal with the CrysAlisPRO software. We collected reflections for determination of the orientation matrix using a four-circle  $\kappa$  Oxford Gemini diffractometer equipped with an Atlas detector ( $\lambda = 0.71073 \text{ \AA}$ ).

### Collection of mid- and far-IR reflectance spectra

We acquired specular reflectance spectra on the Stony Brook University Vibrational Spectroscopy Laboratory's Nicolet 6700 Fourier transform infrared (FTIR) spectrometer using a FT-30 specular reflectance accessory with incidence and reflection angles of 30° at a spectral sampling of 2  $\text{cm}^{-1}$ . An InfraSpecs wire grid IR polarizer was placed in the beam path for collection of polarized reflectance spectra. For each sample, we measured reflectance spectra for four orientations of the crystal with respect to the incident polarized beam. Depending on whether the *a*- or *c*-axis was more readily identifiable, these orientations were 0°, 45°, 90°, and 110° from the identified crystallographic axis. MIR spectra were collected over a range of 400–4000  $\text{cm}^{-1}$  using a KBr beamsplitter and DTGS detector with a CsI window. Each spectrum is an average of 256 scans. Far-IR (FIR) spectra were acquired from 250–600  $\text{cm}^{-1}$  using a Nicolet Solid Substrate beamsplitter and a DTGS detector with a polyethylene window. Each of these spectra is an average of 512 scans. The two wavelength ranges are joined at 600  $\text{cm}^{-1}$  using the overlapping region (600–400  $\text{cm}^{-1}$ ) to scale the spectral contrast of the FIR spectra. MIR and FIR spectral contrast varies by up to 10% due to slight differences in measurement conditions and/or a few degree error in crystal orientation. Samples were placed on a holder that acts as a mask, controlling the spot size. We chose the largest spot size that can be completely covered by the polished surface of the sample. The bottom of the sample holders is coated with paraffin soot to reduce stray reflectance off of the holder into the sample chamber. For the smaller spot-sizes (<0.5 cm diameter) we subtracted a spectrum of the sample holder without a sample or standard placed on top. While the sample holder does not affect the mid-IR reflectance, there is a steep upward slope starting at around 400  $\text{cm}^{-1}$ , which rapidly increases from 0.01 to several percent reflectance at ~100  $\text{cm}^{-1}$ .

### Modeling of optical constants

The optical constants ( $n$ ,  $k$ ) are related to the wavelength-dependent dielectric function [ $\epsilon(\lambda)$ ] of the material ( $\tilde{n} = \epsilon^{1/2}$ ). Electron states in non-conducting materials can be modeled as damped harmonic oscillators, which exhibit spring-like behavior (Griffiths 1999). The E-field of the incoming beam acts as a driving force on the oscillators, which have resonant frequencies  $\nu_j$  ( $\text{cm}^{-1}$ ). The parameters  $s_j$  ( $\text{cm}^2$ ),  $\gamma_j$  ( $\text{cm}^{-1}$ ), and  $\epsilon_\infty$  are the oscillator strength, damping coefficient (proportional to the oscillator velocity), and infinite frequency dielectric constant, respectively. These parameters are explained in more detail in the first section of Discussion.

For minerals of orthorhombic and higher symmetry, we can assume that these oscillations occur parallel to the crystallographic axes. In this case, optical constants can

be determined using the approach of Spitzer and Kleinman (1961). Reflectance spectra are acquired for each principal axis with the polarization parallel to each axis. Each spectrum is iteratively fit with estimated values of the oscillator parameters as input.

When a mineral is biaxial and the axes are not orthogonal, the oscillators cannot be assumed to be parallel to the crystallographic axes (Belousov and Pavnich 1978). In a monoclinic material, optical constants with E parallel to the *b*-axis (where the oscillators are parallel to the axis) can be determined in the same manner as the orthorhombic case. In the *a-c* plane, oscillators are coplanar with, but not parallel to the crystallographic axes. To determine the two remaining principle refractive indices, it is necessary to make measurements at three different angles ( $\Omega$ ) with respect to the crystallographic axes in the *a-c* plane (Aronson et al. 1983), with measurements at more angles providing more robust fits. This results in additional oscillator parameters  $\theta_j$  and  $\varphi_j$ . A useful diagram of such an experimental setup is given in Figure 1 of Ivanovski et al. (2007). The principle complex indices of refraction are the eigenvalues of the complex dielectric-permittivity tensor, which can be calculated as follows, where N is the number of oscillators

$$E = (n + ik)^2 = \begin{pmatrix} \epsilon_{\infty xx} & \epsilon_{\infty xy} & \epsilon_{\infty xz} \\ \epsilon_{\infty xy} & \epsilon_{\infty yy} & \epsilon_{\infty yz} \\ \epsilon_{\infty xz} & \epsilon_{\infty yz} & \epsilon_{\infty zz} \end{pmatrix} + \sum_{j=1}^N \frac{s_j}{\nu_j^2 - i\gamma_j\nu - \nu^2} \times \quad (1)$$

$$\begin{pmatrix} \sin^2\theta_j \cos^2\varphi_j & \sin^2\theta_j \sin\varphi_j \cos\varphi_j & \sin\theta_j \cos\theta_j \cos\varphi_j \\ \sin^2\theta_j \sin\varphi_j \cos\varphi_j & \sin^2\theta_j \sin^2\varphi_j & \sin\theta_j \cos\theta_j \sin\varphi_j \\ \sin\theta_j \cos\theta_j \cos\varphi_j & \sin\theta_j \cos\theta_j \sin\varphi_j & \cos^2\theta_j \end{pmatrix}$$

The reflectance spectra for all  $\Omega$  are fit simultaneously. Fixing the *b*-axis as the *z*-axis of the dielectric tensor,  $\epsilon$  needs to be rotated with  $\Omega$ , according to

$$\epsilon = \begin{pmatrix} \cos\Omega & \sin\Omega \\ -\sin\Omega & \cos\Omega \end{pmatrix} \begin{pmatrix} \epsilon_{xx} & \epsilon_{xy} \\ \epsilon_{xy} & \epsilon_{zz} \end{pmatrix} \begin{pmatrix} \cos\Omega & -\sin\Omega \\ \sin\Omega & \cos\Omega \end{pmatrix} \quad (2)$$

Because of the additional complexity in measurement and calculation, optical constants have been derived from single-crystal samples for only a few monoclinic

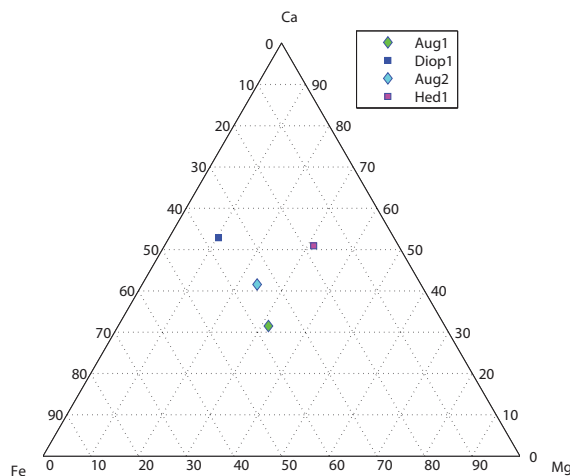


**FIGURE 1.** Ternary of pyroxene compositions included in this study. (Color online.)

materials, including gypsum and orthoclase (Long et al. 1992; Aronson et al. 1983; Aronson 1986). A similar method for triclinic materials is outlined by Aronson et al. (1985). However, substitution of the relevant variables in their equations for the reflection coefficients results in a singularity for the monoclinic case (Mayerhöfer et al. 2010) instead of reducing to the formulas given in Aronson et al. (1983). In addition, the formulation of Aronson et al. applies only to the case of normal incidence. The Berreman 4×4 matrix formulation (Berreman 1972) gives a more consistent approach for calculating the reflectance coefficients in low-symmetry cases (Mayerhöfer and Popp 2007).

Mayerhöfer and Popp (2007) define a matrix  $\tilde{M}$  that can be used to calculate the reflection coefficients as a function of incidence angle ( $\alpha$ ).

$$\tilde{M} = D_{\psi}^{-1}(0) D_{\psi}(1) \quad (3)$$

$$r_{xx} = \frac{\tilde{M}_{21}\tilde{M}_{33} - \tilde{M}_{23}\tilde{M}_{31}}{\tilde{M}_{11}\tilde{M}_{33} - \tilde{M}_{13}\tilde{M}_{31}} \quad (4a)$$

$$r_{xy} = \frac{\tilde{M}_{41}\tilde{M}_{33} - \tilde{M}_{43}\tilde{M}_{31}}{\tilde{M}_{11}\tilde{M}_{33} - \tilde{M}_{13}\tilde{M}_{31}} \quad (4b)$$

$D_{\psi}(0)$  and  $D_{\psi}(1)$  are the dynamical matrices of the incident and refracted waves (Yeh 1979).

$$D_{\psi}^{-1}(0) = \frac{1}{2} \begin{pmatrix} 1 & 1/\text{ncos}\alpha & 0 & 0 \\ 1 & -1/\text{ncos}\alpha & 0 & 0 \\ 0 & 0 & 1/\text{cos}\alpha & 1/n \\ 0 & 0 & -1/\text{cos}\alpha & 1/n \end{pmatrix} \quad (5)$$

$$D_{\psi}(1) = \begin{pmatrix} \epsilon_{xy}(1 - \frac{k_y^2}{\epsilon_{zz}}) & 0 & \epsilon_{xy}(1 - \frac{k_y^2}{\epsilon_{zz}}) & 0 \\ \hat{a}_{xy}(1 - \frac{k_y^2}{\epsilon_{zz}})\gamma_1 & 0 & \epsilon_{xy}(1 - \frac{k_y^2}{\epsilon_{zz}})\gamma_3 & 0 \\ \left(1 - \frac{k_y^2}{\epsilon_{zz}}\right)[\gamma_1^2 - (\epsilon_{xx} - k_y^2)] & 0 & \left(1 - \frac{k_y^2}{\epsilon_{zz}}\right)[\gamma_3^2 - (\epsilon_{xx} - k_y^2)] & 0 \\ [\gamma_1^2 - (\epsilon_{xx} - k_y^2)]\gamma_1 & 0 & [\gamma_3^2 - (\epsilon_{xx} - k_y^2)]\gamma_3 & 0 \end{pmatrix} \quad (6)$$

where  $n$  is the index of refraction of the incident medium,  $k_y$  is the  $y$ -component of the wave-vector (the magnitude and direction of the incoming beam), and

$$\gamma_1 = \sqrt{-\frac{1}{2\epsilon_{zz}}(K_1 + \sqrt{K_1^2 + K_2})} \quad (7a)$$

$$\gamma_3 = \sqrt{\frac{1}{\epsilon_{zz}}(-K_1 + \sqrt{K_1^2 + K_2})} \quad (7b)$$

$$K_1 = -\epsilon_{zz}(\epsilon_{zz} + \epsilon_{yy}) + k_y^2(\epsilon_{yy} + \epsilon_{zz}) \quad (8a)$$

$$K_2 = -4\left[\epsilon_{xy}^2 + \epsilon_{yy}(k_y^2 - \epsilon_{xx})\right](k_y^2 - \epsilon_{zz})\epsilon_{zz}. \quad (8b)$$

To perform the required calculations, we use the Matlab non-linear fitting routine lsqcurvefit, which allows us to set lower and upper bounds, ensuring that the final values for the oscillator parameters are positive. To produce the initial parameters for this model, we first fit the spectrum for each  $\Omega$  as if it is orthorhombic and at normal incidence. The parameters  $v_j$  and  $\gamma_j$  can be estimated reasonably by visual inspection, while  $s_j$  is estimated as in Pavinich and Belousov (1978). Reflectance spectra for all orientations are then fit simultaneously, using the  $\Omega$  where  $s_j$  is the largest for a given  $v_j$  as an initial guess for  $\phi_j$ .

We attempt to fit the reflectance spectrum with the minimum number of oscillators necessary. Starting with the number of main peaks, modes are added until a reasonable fit is obtained for any overlapping peaks or shoulders (a difference between the measured and modeled reflectance of <10%). Sometimes modes can be at the same frequency or very close in frequency, with different  $\theta_j$ . In this case, although there is only one peak, the fit will be poor without an additional oscillator.

### Oscillator parameter error estimates

The model fit is commonly assessed using the standard error of the oscillator parameters. We report the standard error [ $\sigma(v)$ ,  $\sigma(\gamma)$ , etc.] for each parameter in Tables 2–6. This does not reflect the impact of the initial guesses of the oscillator parameters on the final reflectance fit. Poor initial estimates of starting values may result in slow convergence, non-convergence, or convergence on a local rather than global minimum in our model. For each sample, we used five different sets of starting values centered around those produced by the fit to the orthorhombic model to qualitatively evaluate how much the final  $n$  and  $k$  values depended on the initial estimates. Those that gave the best reflectance fit were used to calculate the optical constants. As an additional test, we independently varied the sets of  $v_j$ ,  $\gamma_j$ ,  $s_j$ , and  $\phi_j$  parameters for a gem-quality orthoclase sample to determine which had the largest impact on the final  $n$  and  $k$  values. Large ( $\pm 30 \text{ cm}^{-1}$  for  $v_j$  and  $\pm 50\%$  for all others) variations in the other parameters do not appear to have a major effect on the fit (see Figs. 2–5). Figure 6 shows the final fits when all parameters are varied by these amounts (top) as well the 95% confidence bounds based on the standard error of the parameters (bottom). The two measures of uncertainty appear to diverge from the calculated optical constants at different wavenumbers.

## RESULTS

For each sample we present the measured and modeled reflectance and the plots of  $n$  and  $k$  as a function of wavelength derived from the reflectance fit. The measured and modeled spectra, as well as the derived optical constants and oscillator parameters are available at [http://aram.ess.sunysb.edu/tglotch/optical\\_constants.html](http://aram.ess.sunysb.edu/tglotch/optical_constants.html).

### Augite 1

Measured reflectance and model are shown in Figure 7, with incident E-field polarization parallel to the  $a$ - $c$  plane (top three) and parallel to  $b$  (bottom). Derived values of  $n$  and  $k$  are shown in Figure 8. In Figure 8,  $n_1, n_2$  and  $k_1, k_2$  are the optical constants for the rays whose polarization direction is parallel to the  $a$ - $c$  plane, while  $n_b$  and  $k_b$  are the optical constants for the rays with polarization direction along the  $b$  crystallographic axis. Oscillator parameters for this sample are given in Table 2.

### Augite 2

Measured reflectance and model are shown in Figure 9, with incident E-field polarization parallel to the  $a$ - $c$  plane (top three) and parallel to  $b$  (bottom). Derived values of  $n$  and  $k$  are given in Figure 10. In Figure 10,  $n_1, n_2$  and  $k_1, k_2$  are the optical constants for the rays whose polarization direction is parallel to the  $a$ - $c$  plane, while  $n_b$  and  $k_b$  are the optical constants for the rays with polarization direction along the  $b$  crystallographic axis. Oscillator parameters for this sample are given in Table 3.

### Diopside

Measured reflectance and model are shown in Figure 11, with incident E-field polarization parallel to the  $a$ - $c$  plane (top three) and parallel to  $b$  (bottom). Derived values of  $n$  and  $k$  are shown in Figure 12. In Figure 12,  $n_1, n_2$  and  $k_1, k_2$  are the optical constants for the rays whose polarization direction is parallel to the  $a$ - $c$  plane, while  $n_b$  and  $k_b$  are the optical constants for the rays with polarization direction along the  $b$  crystallographic axis. Oscillator parameters for this sample are given in Table 4.

**TABLE 2.** Oscillator parameters for Augite (Aug1)

<i>j</i>	$\nu_j$	$\sigma(\nu_j)$	$\gamma_j$	$\sigma(\gamma_j)$	$s_j$	$\sigma(s_j)$	$\phi_j$	$\sigma(\phi_j)$	$\theta_j$
1	1106.3575	0.4039	13.6440	1.4160	4710.7187	519.6075	33.7390	2.2315	90
2	1082.0787	0.7336	22.4311	2.8987	8993.4843	1526.8844	57.9436	2.2866	90
3	1049.0371	0.1930	34.2430	0.6058	179324.6400	2855.2145	71.6003	0.2040	90
4	1010.1750	0.5134	20.6827	1.4914	15743.7790	1164.9098	33.9720	1.4204	90
5	973.9422	1.2439	39.3002	2.5816	61647.1074	7198.6643	100.6033	1.9936	90
6	952.8605	0.6238	33.8723	1.1586	115080.9250	3657.2602	76.5908	1.6294	90
7	911.9700	1.9049	60.9354	5.4555	84647.1159	6815.1152	69.0827	1.9607	90
8	944.8770	0.6580	48.8271	2.4135	96156.4057	6739.0871	130.0419	2.5202	90
9	864.4122	0.4977	43.8169	1.0250	236251.8770	364.8184	1.5422	0.5618	90
10	855.2310	0.9153	31.8268	2.0963	73587.6460	1012.5941	148.5916	2.1071	90
11	768.1230	1.8893	89.4754	7.2442	55510.9508	4229.1492	106.3017	2.6079	90
12	628.8353	0.2212	18.0435	0.7495	33689.7859	1649.9417	101.0689	0.8103	90
13	558.8928	0.5426	20.5635	1.7036	3907.3075	383.2433	-1.2976	4.3107	90
14	527.2604	0.5724	24.0277	2.0407	10163.0101	1027.2230	2.9381	3.4734	90
15	511.0346	0.6194	42.7838	2.2268	48307.6346	3153.4361	113.9736	1.4942	90
16	588.4716	5.8446	86.0548	18.4170	24961.4935	5574.7554	89.6034	3.3377	90
17	487.9342	0.3804	27.1740	1.2809	59799.8695	3570.4805	-7.2227	0.8682	90
18	452.2373	0.2418	29.8619	0.7627	256324.4190	4869.1466	-7.2227	0.1871	90
19	378.5617	0.2780	36.6437	1.4695	53084.6470	8107.2438	84.8518	6.4041	90
20	380.5842	1.0044	53.7977	4.0509	72332.4613	6006.1467	25.3526	6.0986	90
21	316.6041	0.1706	22.8939	0.3635	121807.2190	1236.6558	76.0592	0.3385	90
22	285.8952	0.3018	26.1164	0.7252	78823.7304	1650.5374	141.5585	0.5527	90
23	1066.2639	0.1892	30.6764	0.2559	222090.2320	1434.7913	0	-	0
24	963.3500	0.2452	24.6545	0.6687	89492.5772	2397.4128	0	-	0
25	900.8600	0.5216	61.1955	1.6569	210326.1180	4518.3363	0	-	0
26	673.6817	1.2406	34.7883	3.7145	19978.7527	1653.7995	0	-	0
27	547.9000	0.4589	18.9619	1.7624	6433.4126	786.4962	0	-	0
28	503.9100	0.2723	37.6983	0.8500	148239.2660	4230.4820	0	-	0
29	473.3900	0.2018	18.3338	0.6366	104023.2710	2914.9693	0	-	0
30	408.0200	0.4402	21.1392	1.4232	26911.5056	1472.1208	0	-	0
31	367.1695	1.0108	22.6618	4.1379	12240.3510	2468.8277	0	-	0
32	333.8303	0.7396	37.0955	2.4841	44673.8703	2939.0821	0	-	0

$\epsilon_{xx} = 2.3418(0.0040)$   $\epsilon_{xy} = 0.0263(0.0036)$   $\epsilon_{yy} = 2.3934(0.0030)$   $\epsilon_{zz} = 2.6441(0.0043)$

Notes: The parameters  $\nu$ ,  $\gamma$ ,  $s$ ,  $\phi$ , and  $\theta$  are those described in the Discussion section. The standard error,  $\sigma$ , is given for each parameter.

**TABLE 3.** Oscillator parameters for Augite (Aug2)

<i>j</i>	$\nu_j$	$\sigma(\nu_j)$	$\gamma_j$	$\sigma(\gamma_j)$	$s_j$	$\sigma(s_j)$	$\phi_j$	$\sigma(\phi_j)$	$\theta_j$
1	1061.3863	1.6775	16.7945	3.5355	24107.2736	9108.7181	109.9541	3.0586	90
2	1045.6266	1.0695	17.4601	4.5891	49146.8143	15451.7954	118.8724	1.4748	90
3	1021.4581	1.8514	25.7043	6.2705	46430.9850	12385.4430	125.3247	2.1043	90
4	992.3639	1.1743	36.2713	3.4181	26819.2312	2845.9399	4.0808	7.8728	90
5	950.6749	1.8544	56.3535	3.6006	350600.2530	198.6376	92.4733	1.0478	90
6	873.6918	3.5412	73.3247	7.0740	198501.9250	4841.0644	103.9087	5.7859	90
7	852.6279	0.9302	56.1304	2.4576	384449.5580	21164.2827	-0.0526	2.7969	90
8	768.7863	3.5090	100.1498	11.8050	351227.4630	80.4223	-35.0603	1.7465	90
9	600.0011	3.0444	103.2869	9.5882	345195.2700	27533.1404	-49.3688	1.6754	90
10	686.4430	3.5464	112.2921	13.4456	157635.0660	22704.7234	15.7006	3.6531	90
11	625.9819	1.2538	25.3481	4.3195	31759.5593	5445.8591	73.3052	5.5194	90
12	520.0000	1.4388	20.2592	3.8818	55527.2990	8895.0274	82.9539	8.5934	90
13	533.0903	2.2436	17.2663	6.5846	26237.0233	1283.3818	179.8287	8.5146	90
14	501.7328	1.5229	22.9771	4.8641	168521.7630	27.0692	8.2681	4.3965	90
15	479.9509	0.7686	16.6904	2.6651	294597.8250	25.7761	4.6831	2.0602	90
16	461.8681	0.8220	14.9005	1.5448	258672.0850	1733.0123	5.0887	1.8157	90
17	403.8875	1.6247	34.3784	4.1294	86703.4089	6799.8357	99.5010	4.3104	90
18	360.1886	6.2701	27.2829	19.1020	17351.0619	11466.8151	-7.5571	14.6287	90
19	332.0028	1.0169	21.7865	3.0345	38951.2369	4767.2072	72.8595	5.0749	90
20	281.8601	1.4334	41.1500	3.7859	226289.1590	41.8564	32.8478	1.1554	90
21	250.0777	4.5801	15.2753	5.7124	41555.6458	23085.6849	74.3621	10.3421	90
22	1077.2920	0.4198	22.8731	0.6367	149503.0950	2402.3553	0	-	0
23	964.0978	1.2006	48.8749	4.5997	138155.7890	15182.2000	0	-	0
24	899.9383	3.5474	106.4168	7.3552	286332.2180	24390.6181	0	-	0
25	684.1713	5.8182	108.5547	25.4532	66276.4418	26720.9365	0	-	0
26	557.1254	1047.5670	15.2229	666.7554	3104.1971	177321.3230	0	-	0
27	541.0487	3.4361	17.7469	31.3527	9273.8041	161727.1810	0	-	0
28	524.2434	1.6431	18.0151	10.7360	19617.9937	16815.8158	0	-	0
29	507.6945	0.5276	18.0932	2.3374	67758.0486	12997.2329	0	-	0
30	480.6085	0.8391	31.0358	2.9332	173741.2560	16787.0322	0	-	0
31	411.3853	5.8307	45.1586	20.6277	61591.7484	47708.6593	0	-	0
32	370.1525	19.3001	44.4246	135.0416	23586.7622	91495.5373	0	-	0
33	325.5302	12.2621	65.4127	22.8392	72943.9747	51540.5930	0	-	0
34	257.0514	0.9801	12.4295	2.7168	16853.4601	3824.3130	0	-	0

$\epsilon_{xx} = 3.1888(0.0147)$   $\epsilon_{xy} = 0.0050(0.0168)$   $\epsilon_{yy} = 2.8116(0.0157)$   $\epsilon_{zz} = 2.6090(0.0109)$

Notes: The parameters  $\nu$ ,  $\gamma$ ,  $s$ ,  $\phi$ , and  $\theta$  are those described in the Discussion section. The standard error,  $\sigma$ , is given for each parameter.

**TABLE 4.** Oscillator parameters for Diopside (Diop1)

<i>j</i>	<i>v<sub>j</sub></i>	$\sigma(v_j)$	$\gamma_j$	$\sigma(\gamma_j)$	<i>s<sub>j</sub></i>	$\sigma(s_j)$	$\phi_j$	$\sigma(\phi_j)$	$\theta_j$
1	1053.3492	0.2690	9.8041	0.5202	161807.4260	8449.4644	95.0619	0.5386	90
2	1038.6875	0.4434	11.9789	1.1319	102002.5840	8297.6460	81.8839	0.7175	90
3	987.1730	1.1344	22.0697	2.3375	43276.2855	8424.1418	-58.3177	1.7571	90
4	961.9418	0.5321	21.8740	1.4044	328246.2610	13426.1056	107.2574	0.4212	90
5	908.9778	1.2771	34.1717	3.7573	112024.9180	10847.7536	88.2555	1.2813	90
6	851.9349	0.7393	52.0897	1.8660	276075.0410	8603.7134	40.6706	1.1639	90
7	799.5717	2.9359	82.3099	8.5987	133499.1160	11910.3499	140.7057	2.6738	90
8	694.3785	2.9357	139.0056	9.4790	184063.9650	11455.4558	35.9865	1.6679	90
9	625.9676	0.6184	20.9614	1.1518	85562.6394	3066.4869	111.9229	0.8129	90
10	526.8297	1.7909	48.7469	3.7816	97271.7196	11572.2554	45.1962	1.4457	90
11	509.9354	0.7947	14.1122	2.1296	16820.8129	2318.7730	-38.9575	4.1582	90
12	488.7702	1.0874	25.2207	3.2101	102617.7860	14753.3418	51.9415	1.9863	90
13	462.0420	0.8680	37.2480	2.3266	302939.5670	16231.8191	21.2456	0.8955	90
14	379.4407	0.6114	32.5722	1.2839	117538.4980	4685.8259	112.1053	0.9140	90
15	326.4878	0.9753	26.4854	2.6635	108243.6900	14930.1059	-66.8801	1.1360	90
16	297.4023	1.4361	27.9642	5.2131	98661.8029	17147.5147	-59.4064	4.2180	90
17	293.0303	0.7230	16.9140	1.9692	26130.5743	3123.2116	20.9335	12.1318	90
18	236.8182	2.6280	14.3421	3.0202	49054.5289	8115.4718	10.1390	6.1075	90
19	1065.2649	61.4940	50.5334	1.8536	136867.0000	139.1562	0	-	0
20	954.2127	50.9689	35.3480	3.5371	65646.0001	54.6979	0	-	0
21	913.3331	114.3238	31.7870	6.9236	42070.0001	24.6549	0	-	0
22	863.7441	367.8407	126.8820	24.7606	195784.2720	54551.0765	0	-	0
23	737.9597	2678.3443	140.9497	56.2231	92809.1745	52723.1287	0	-	0
24	636.0029	552.8693	93.0399	9.7740	89888.9079	17968.0509	0	-	0
25	504.2384	645.0038	31.7429	1.4460	163435.8470	13745.7938	0	-	0
26	472.0973	792.9559	28.4750	1.9606	276342.9090	15861.7259	0	-	0
27	413.8197	324.9801	26.0624	3.2501	70136.7282	7278.4287	0	-	0
28	249.2397	277.7731	9.7763	1.2649	18139.7810	2824.9225	0	-	0

$\epsilon_{xx} = 2.2120(0.0092)$   $\epsilon_{yy} = 0.0084(0.0109)$   $\epsilon_{zz} = 3.2076(0.0107)$   $\epsilon_{xy} = 2.3310(0.0111)$

Notes: The parameters *v*,  $\gamma$ , *s*,  $\phi$  and  $\theta$  are those described in the Discussion section. The standard error,  $\sigma$ , is given for each parameter.

**TABLE 5.** Oscillator parameters for Hedenbergite (Hed1)

<i>j</i>	<i>v<sub>j</sub></i>	$\sigma(v_j)$	$\gamma_j$	$\sigma(\gamma_j)$	<i>s<sub>j</sub></i>	$\sigma(s_j)$	$\phi_j$	$\sigma(\phi_j)$	$\theta_j$
1	1085.5086	1.0619	53.6032	2.0797	71057.9148	10.0624	77.0368	1.6560	90
2	1059.2960	0.5518	45.6650	1.1514	159377.0460	3792.4402	-48.5292	0.5769	90
3	993.1131	1.1689	26.9090	3.5555	9922.7969	2381.2746	38.0265	7.7690	90
4	967.4469	0.8350	45.8181	2.5602	95361.6473	4969.2601	84.6362	1.1185	90
5	904.4503	1.5764	39.7557	4.0140	17736.2350	2895.3918	9.7179	4.8795	90
6	854.4819	0.3215	34.8501	0.7845	359324.3050	3685.3273	8.2315	0.2746	90
7	627.1273	0.4077	18.5918	0.9474	22454.7292	809.0312	70.7968	1.0661	90
8	554.0051	0.8223	20.0375	2.2529	11125.4731	935.6338	80.3744	1.5719	90
9	498.4405	0.5100	36.7979	1.1952	47045.1989	1737.4115	31.5953	0.6441	90
10	444.5136	0.2360	25.4438	0.5064	259681.5030	2531.5769	7.0115	0.1641	90
11	365.7561	0.4065	40.0052	1.1436	115793.2740	2579.3708	-17.1310	0.3263	90
12	316.5364	0.2868	17.5481	0.7074	79478.0308	2327.4479	146.8989	0.4168	90
13	295.8607	0.2829	11.2035	0.8214	38037.8982	2341.3446	-10.7030	0.9746	90
14	269.8787	0.2434	11.4372	0.5673	24979.2863	1003.2629	31.7790	0.9470	90
15	1058.5000	0.1466	13.5591	0.1493	298081.4700	1586.6960	0	-	0
16	954.2000	0.1756	15.9576	0.3435	155456.8690	2858.5771	0	-	0
17	905.3000	0.3818	37.5829	1.0258	283403.9260	5357.2963	0	-	0
18	661.1000	1.2062	61.1123	3.4700	68518.4267	3042.9618	0	-	0
19	509.4000	0.2300	25.7632	0.3148	236134.3190	3062.6966	0	-	0
20	471.8000	0.2540	14.0770	0.6940	81073.6183	2729.1871	0	-	0
21	398.1000	0.3743	23.0772	1.0692	64178.4958	2420.5236	0	-	0
22	363.7127	0.6361	14.3740	2.4526	17497.1025	3048.7496	0	-	0
23	330.9739	1.4859	43.8902	5.1669	49615.4221	5331.1122	0	-	0
24	277.0999	0.3965	9.3079	1.2061	11291.1774	1162.9514	0	-	0

$\epsilon_{xx} = 2.323433(0.005738)$   $\epsilon_{yy} = 0.011083(0.004933)$   $\epsilon_{zz} = 1.811383(0.004054)$   $\epsilon_{xy} = 3.476333(0.0063)$

Notes: The parameters *v*,  $\gamma$ , *s*,  $\phi$  and  $\theta$  are those described in the Discussion section. The standard error,  $\sigma$ , is given for each parameter.

**Hedenbergite**

Measured reflectance and model are shown in Figure 13, with incident E-field polarization parallel to the *a-c* plane (top three) and parallel to *b* (bottom). Derived values of *n* and *k* are shown in Figure 14. In Figure 14, *n*<sub>1</sub>,*n*<sub>2</sub> and *k*<sub>1</sub>,*k*<sub>2</sub> are the optical constants for the rays whose polarization direction is parallel to the *a-c* plane, while *n*<sub>b</sub> and *k*<sub>b</sub> are the optical constants for the rays with polarization direction along the *b* crystallographic axis. Oscillator parameters for this sample are given in Table 5.

**Orthoclase**

Measured reflectance and model are shown in Figure 15, with incident E-field polarization parallel to the *a-c* plane (top three) and parallel to *b* (bottom). Derived values of *n* and *k* are shown in Figure 16 as well as those from Aronson (1986). In Figure 16, *n*<sub>1</sub>,*n*<sub>2</sub> and *k*<sub>1</sub>,*k*<sub>2</sub> are the optical constants for the rays whose polarization direction is parallel to the *a-c* plane, while *n*<sub>b</sub> and *k*<sub>b</sub> are the optical constants for the rays with polarization direction along the *b* crystallographic axis. Oscillator parameters for this sample are given in Table 6.

**TABLE 6.** Oscillator parameters for Orthoclase (Orth1)

$j$	$\nu_j$	$\sigma(\nu_j)$	$\gamma_j$	$\sigma(\gamma_j)$	$s_j$	$\sigma(s_j)$	$\phi_j$	$\sigma(\phi_j)$	$\theta_j$
1	1128.3686	0.3431	31.2995	0.7423	54556.3167	2123.2030	144.4339	1.2192	90
2	1108.8571	0.5588	31.1108	0.5308	212226.6890	3795.8550	24.3628	0.4137	90
3	1027.3708	0.3793	33.1247	0.6044	363554.0780	18.0570	96.9297	1.5021	90
4	1037.7416	0.5378	30.7390	1.3144	141912.7300	17.9877	4.6421	2.7087	90
5	1009.9518	0.4677	22.2564	1.0482	172752.3130	5177.9700	175.9980	1.8392	90
6	991.7254	0.5793	24.2304	2.0259	150428.1450	11517.6300	103.3195	1.8847	90
7	765.4734	3.4041	42.0367	10.9087	15482.5298	3241.5640	5.9023	6.1221	90
8	718.5118	1.2856	27.2765	3.9460	20263.4125	2306.1400	-51.0158	3.5496	90
9	638.1094	0.4900	17.9200	1.1941	28666.8966	1392.3170	145.0234	1.2033	90
10	578.8337	1.6291	24.5589	1.0170	42223.7579	9406.2510	43.3327	1.7890	90
11	570.6447	0.5394	11.6388	0.7779	73786.7114	488.4382	42.3799	1.2196	90
12	563.4729	0.7157	9.2861	1.9959	35232.0422	9229.9400	39.1535	2.2532	90
13	415.7642	0.5353	34.7887	0.7423	114579.3000	1911.6290	-41.7658	0.4592	90
14	1135.3801	0.8506	39.8303	2.1129	14854.1612	1579.1328	0	-	0
15	1102.8937	0.5060	42.5629	2.0172	32799.5356	2104.3277	0	-	0
16	1020.6898	0.5366	42.7108	0.7767	259002.7780	13008.0113	0	-	0
17	992.4225	0.2744	32.1287	0.8942	387229.1360	12639.2520	0	-	0
28	774.4806	1.3876	22.3337	4.0335	15639.1124	4074.5787	0	-	0
19	752.3726	1.4388	23.5478	7.5651	15823.7692	6397.6618	0	-	0
20	725.7595	1.3542	25.5395	3.9808	18424.9031	3558.0395	0	-	0
21	610.5486	0.5855	17.5118	1.7004	11599.0969	836.4948	0	-	0
22	543.0700	0.2560	16.9498	0.6631	31705.6149	1032.8273	0	-	0

$$\epsilon_{xx} = 2.0658(0.0111) \quad \epsilon_{xy} = 0.0043(0.0085) \quad \epsilon_{yy} = 2.0126(0.0107) \quad \epsilon_{zz} = 2.4461(0.0033)$$

Notes: The parameters  $\nu$ ,  $\gamma$ ,  $s$ ,  $\phi$ , and  $\theta$  are those described in the Discussion section. The standard error,  $\sigma$ , is given for each parameter.

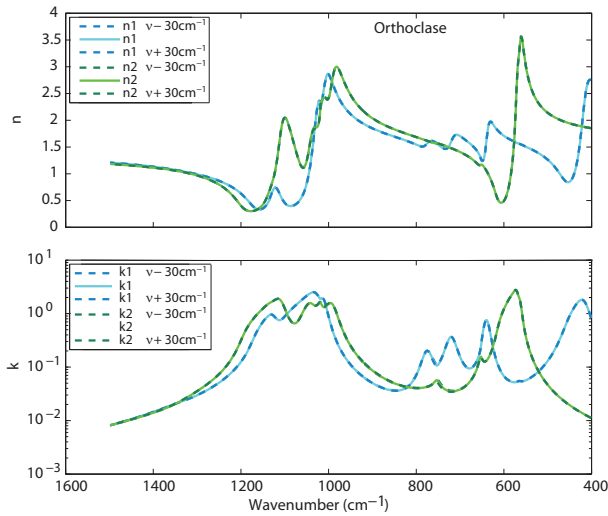


**FIGURE 2.** Changes in modeled optical constants ( $n$ ,  $k$ ) of orthoclase with initial estimates of  $\nu_j$  shifted by  $30 \text{ cm}^{-1}$ . (Color online.)

## DISCUSSION

### Interpretation of dispersion parameters

The optical constants  $n$  and  $k$  are related to the polarizability ( $\alpha$ ), the dependence of the magnitude of the dipole moment on an applied electric field, and conductivity ( $\sigma$ ), the ability of a material to carry a current, which are both properties of the material. The dependence of the polarizability and conductivity and hence the optical constants on wavelength are given by dispersion relations. To derive these dispersion relations, Lorentz postulated that insulating materials contain electrons that are bound to atoms or molecules by Hooke's law forces (Seitz 1940), so that the binding force is proportional to the charge displacement. The motion of the bound electron is described as a harmonic oscillator subject to a periodic electric field ( $\mathbf{E} = \mathbf{E}_0 e^{-2\pi i \nu t}$ ) and damped by a force proportional to the electron's velocity [ $m_e \gamma (dx/dt)$ ] giving:

$$\frac{d^2 x}{dt^2} + 2\pi\gamma \frac{dx}{dt} + 4\pi^2 \nu_0^2 x = \frac{-q_e}{m_e} E_0 e^{2\pi i \nu t} \quad (9)$$

$$x = \frac{q_e}{4\pi^2 m_e} \frac{E_0 e^{-2\pi i \nu t}}{\nu_0^2 - \nu^2 - i\gamma\nu} \quad (10)$$

The resonant frequency of the oscillator is  $\nu_0$  and the damping constant is  $2\pi m_e \gamma$ . As  $\nu$  passes through the value  $\nu_0$ , there is a peak in the absorption coefficient with a half-width of roughly  $\gamma$ . The order of magnitude of can be estimated by the following (Seitz 1940)

$$\gamma \sim \frac{4\pi\nu^2 q_e^2}{3m_e c} \quad (11)$$

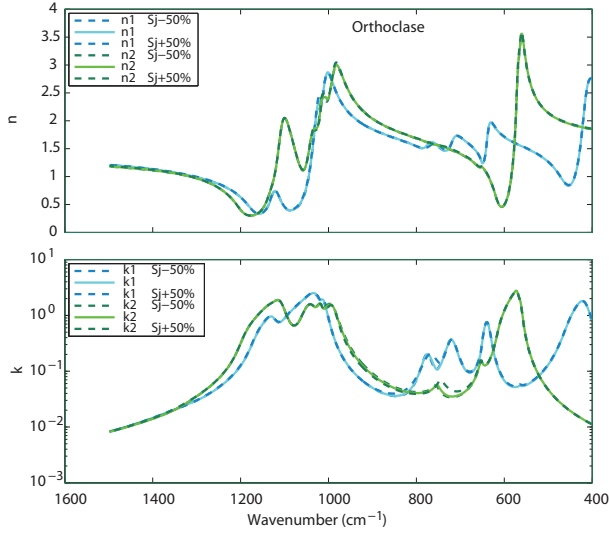


FIGURE 4. Changes in modeled optical constants ( $n$ ,  $k$ ) of orthoclase with initial estimates of  $s_j$  shifted by  $\pm 50\%$ . (Color online.)

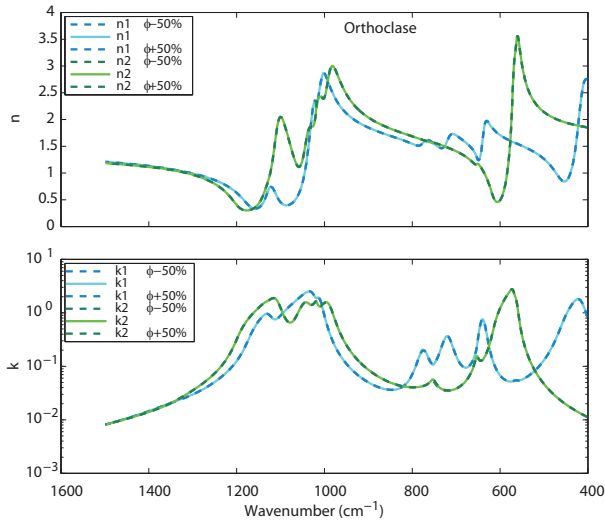


FIGURE 5. Changes in modeled optical constants ( $n$ ,  $k$ ) of orthoclase with initial estimates of  $\phi_j$  shifted by  $\pm 50\%$ . (Color online.)

where  $q_e$  is in statcoulombs,  $\nu$  is in wavenumbers,  $m_e$  is in grams, and  $c$  is in cm/s. Looking at Equation 10 and assuming the dipole moment has a linear response to the electric field ( $\mathbf{p} = \epsilon_0 \alpha \mathbf{E}$ ), results in

$$\alpha = \frac{q_e^2}{4\pi^2 m_e s_0} \frac{1}{\nu_0^2 - \nu^2 - i\gamma\nu} \quad (12)$$

Using a form of the Clausius-Mosotti relation  $\epsilon = \epsilon_\infty + 4\pi N\alpha = \epsilon_\infty + 4\pi N\alpha$  (Spitzer et al. 1959) gives the dispersion relation for a single resonance.

Of course, for a given material, there will not be just one resonant frequency, but several  $\nu_j$  each with a different damping constant  $\gamma_j$ . The quantum mechanical approach to this problem deals with this and also gives one additional parameter oscillator “strength” ( $f_j$ ), a weighting for each oscillator that relates to

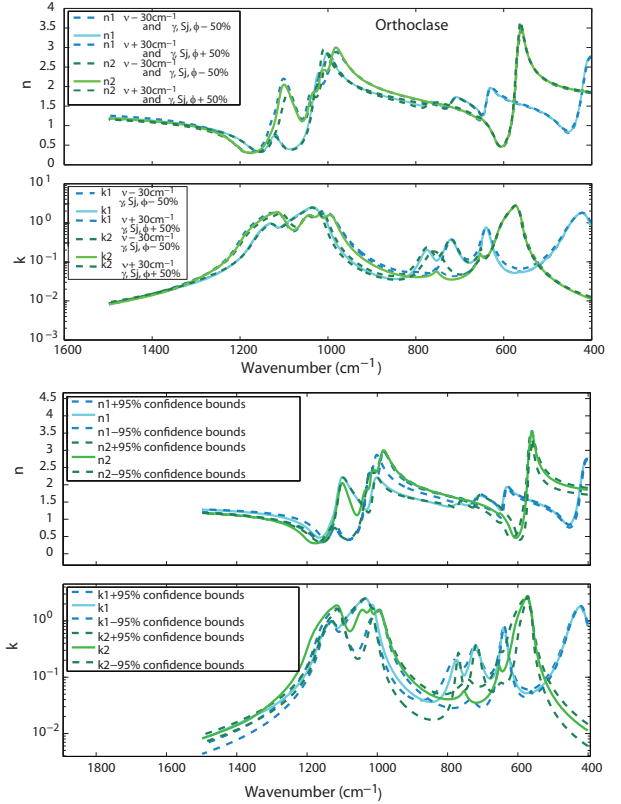


FIGURE 6. Changes in modeled optical constants ( $n$ ,  $k$ ) of orthoclase with initial estimates of  $\nu_j$ ,  $\gamma_j$ ,  $s_j$ , and  $\phi_j$  shifted by  $\pm 50\%$  (top). (Color online.)

the absorption or transition probability (Seitz 1940; Spitzer and Kleinman 1961; Born and Wolf 1999). The parameter  $s_j$  used in Equation 1 can be defined in terms of  $f_j$  as shown in Spitzer and Kleinman (1961).

$$s_j = 4\pi\rho_j\nu_j^2 = \frac{Nq_e^2}{\pi m_e} f_j \quad (13)$$

While educated guesses can be made, the oscillator parameters ( $\nu_j$ ,  $\gamma_j$ , and  $s_j$ ) are difficult to derive exactly from first principles, which is why an iterative technique is normally used. The infinite frequency dielectric constant  $\epsilon_\infty$  can be estimated from the square of the visible-wavelength index of refraction (Roush et al. 1991).

### Comparison with previously derived orthoclase optical constants

Optical constants for orthoclase have been derived from oriented single-crystal reflectance spectra by Aronson (1986). Figure 16 shows the values found in this study along with those from Aronson (1986). The optical constants for the E-field polarization parallel to b orientation (nb and kb) are very similar, while the optical constants (n1, n2 and k1, k2) for the E-field parallel to the a-c plane have slight differences. Variations between the two data sets may be due to either compositional differences in the samples or uncertainties in orientation. Our orthoclase sample had a small amount of Fe<sup>3+</sup> substituting for Al<sup>3+</sup> (see Table 1).

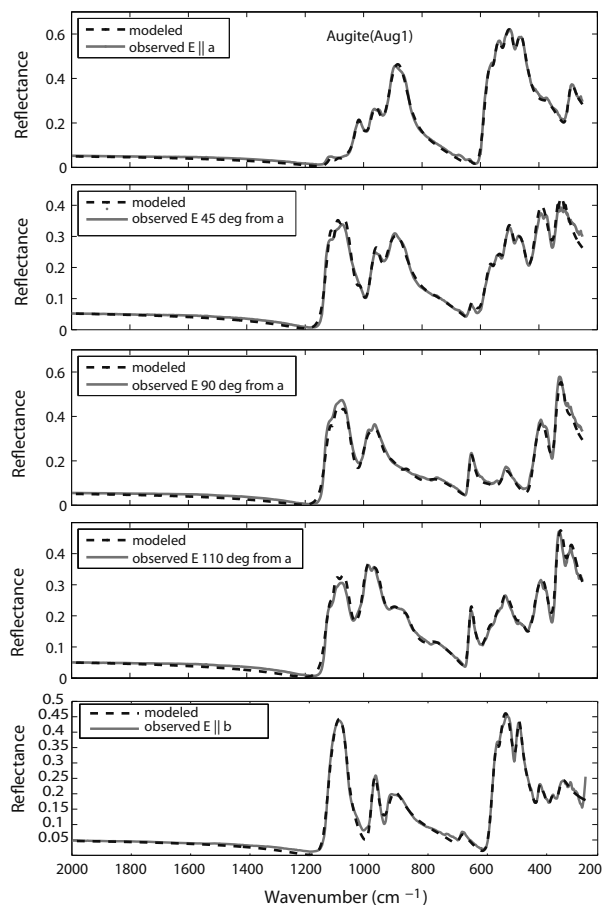


FIGURE 7. Measured and modeled reflectance spectra of augite (Aug1) with incident E-field polarization parallel to *a-c* plane at different polarization angles  $\phi$  (top four) and parallel to *b* (bottom).

However, without any compositional information on the sample used in the Aronson (1986) study, it is difficult to make inferences about specific bands.

#### Dependence of optical constants on crystal structure and chemistry

Isometric minerals will have one set of optical constants for each wavelength. Because most minerals are anisotropic, the polarizability and conductivity will be directionally as well as wavelength dependent and therefore so will the optical constants. Dispersion in uniaxial and biaxial minerals is described by a dielectric tensor rather than just a dielectric constant. The number of oscillator parameters necessary to fit the reflectance spectrum generally increases with decreasing crystal symmetry. Figure 17 shows averaged optical constants in the MIR for several minerals that belong to different crystal systems. It is also important to measure optical constants for several different chemical compositions within the same mineral group. As shown in this work, optical constants vary considerably with chemistry. Simply using one composition of olivine, for example, may produce poor fits for mineralogical abundance as shown in Liu (2012) at VNIR wavelengths.

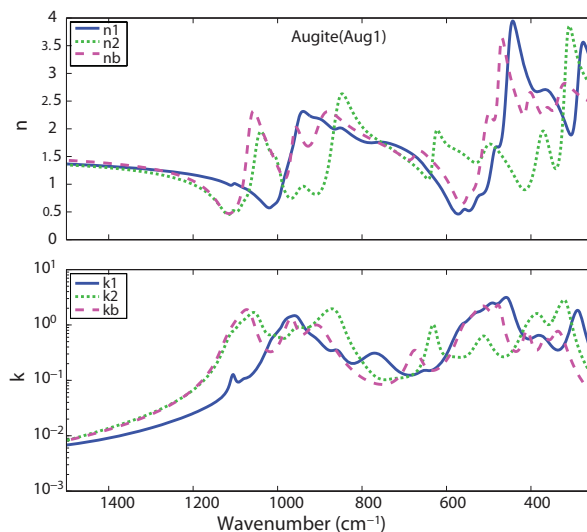


FIGURE 8. Optical constants ( $n$ ,  $k$ ) of augite (Aug1). In this figure,  $n_1$ ,  $n_2$  and  $k_1$ ,  $k_2$  are the optical constants for the rays whose polarization direction is parallel to the *a-c* plane, while  $n_b$  and  $k_b$  are the optical constants for the rays with polarization direction along the *b* crystallographic axis. (Color online.)

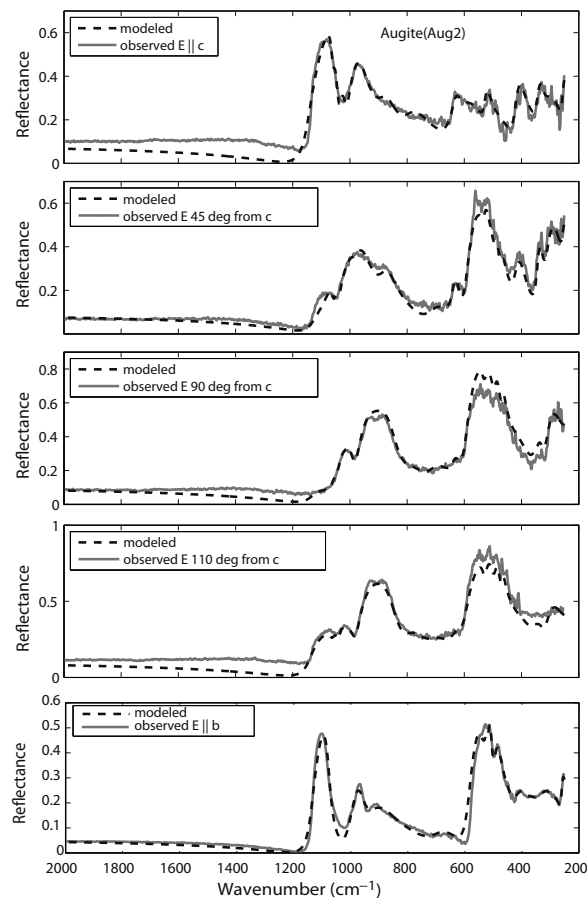
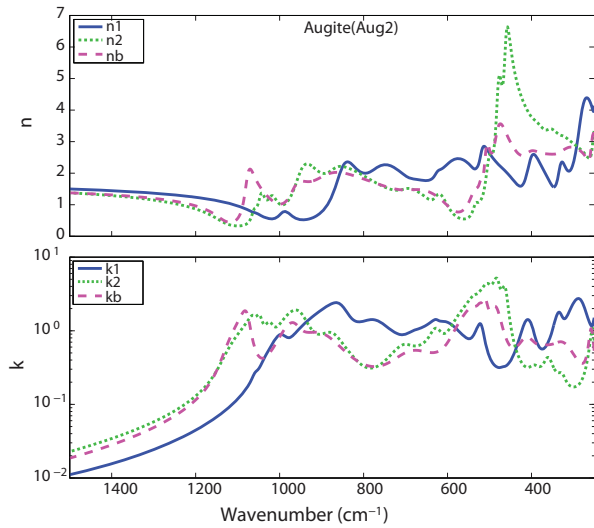
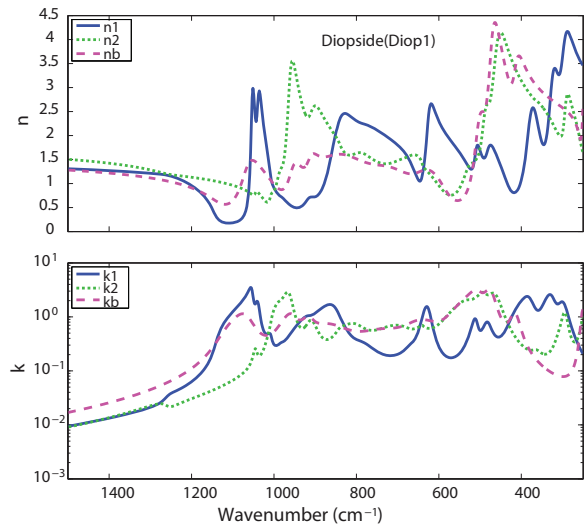


FIGURE 9. Measured and modeled reflectance spectra of augite (Aug2) with incident E-field polarization parallel to *a-c* plane at different polarization angles  $\phi$  (top four) and parallel to *b* (bottom).



**FIGURE 10.** Optical constants ( $n, k$ ) of augite (Aug2). In this figure,  $n_1, n_2$  and  $k_1, k_2$  are the optical constants for the rays whose polarization direction is parallel to the  $a$ - $c$  plane, while  $n_b$  and  $k_b$  are the optical constants for the rays with polarization direction along the  $b$  crystallographic axis. (Color online.)



**FIGURE 12.** Optical constants ( $n, k$ ) of diopside (Diop1). In this figure,  $n_1, n_2$  and  $k_1, k_2$  are the optical constants for the rays whose polarization direction is parallel to the  $a$ - $c$  plane, while  $n_b$  and  $k_b$  are the optical constants for the rays with polarization direction along the  $b$  crystallographic axis. (Color online.)

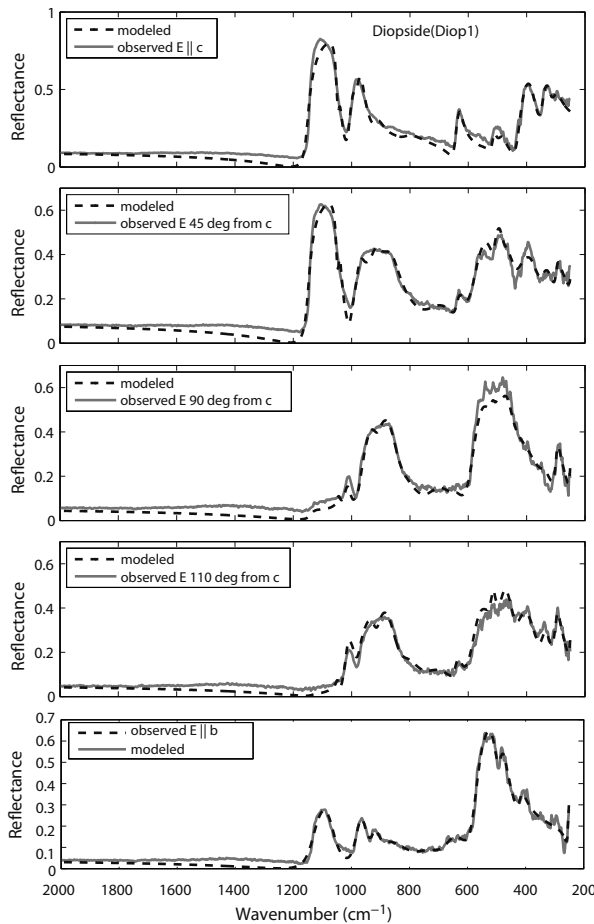


**FIGURE 11.** Measured and modeled reflectance spectra of diopside (Diop1) with incident E-field polarization parallel to  $a$ - $c$  plane at different polarization angles  $\phi$  (top four) and parallel to  $b$  (bottom).

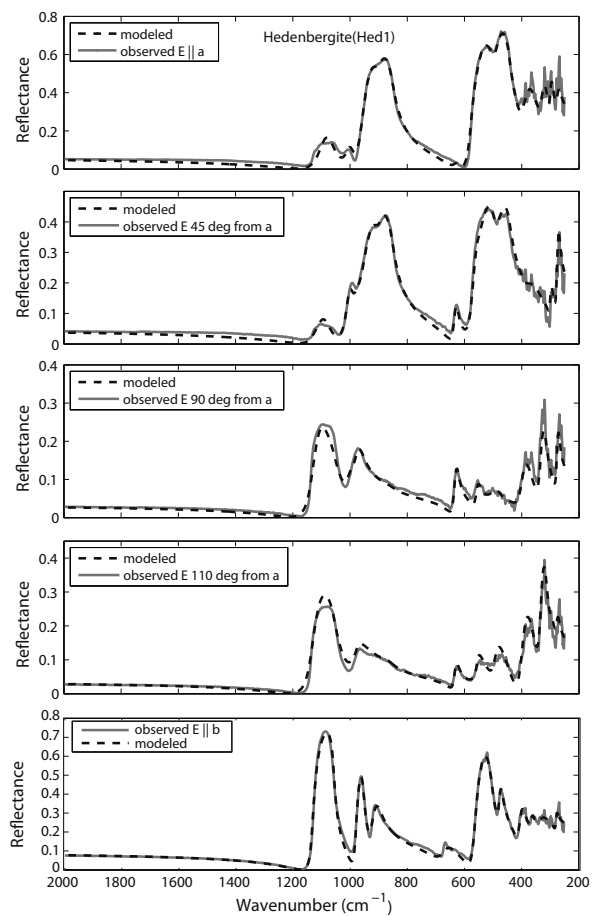


**FIGURE 13.** Measured and modeled reflectance spectra of hedenbergite (Hed1) with incident E-field polarization parallel to  $a$ - $c$  plane at different polarization angles  $\phi$  (top four) and parallel to  $b$  (bottom).

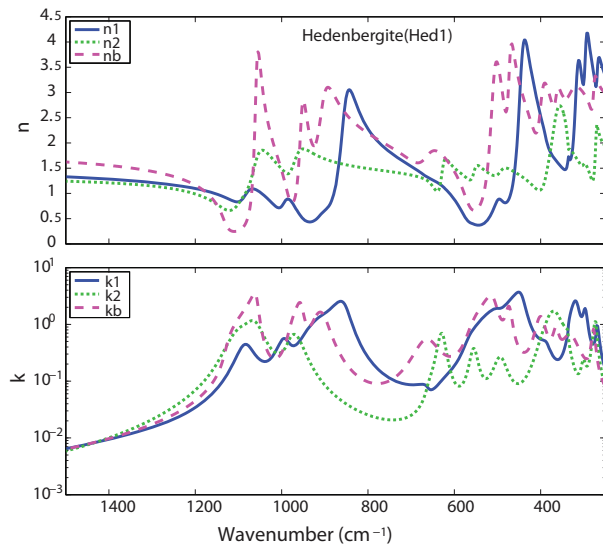


**FIGURE 14.** Optical constants ( $n$ ,  $k$ ) of hedenbergite (Hed1). In this figure,  $n_1, n_2$  and  $k_1, k_2$  are the optical constants for the rays whose polarization direction is parallel to the  $a$ - $c$  plane, while  $n_b$  and  $k_b$  are the optical constants for the rays with polarization direction along the  $b$  crystallographic axis. (Color online.)

For silicates, there is a steep absorption edge in the UV-range after which  $k$ -values drop by orders of magnitude and remain low through the VNIR. As a result, after the UV-edge, dispersion is low until the MIR, where the fundamental vibrational bands occur. There is a steep rise in  $k$  between 8 and 10  $\mu\text{m}$  (1250–1000  $\text{cm}^{-1}$ ), with the maximum  $k$  occurring where  $n = 1$  or slightly lower than 1. This is known as the Christiansen feature and is associated with a minimum in reflectance and a maximum in emission. This feature is the means by which Diviner data are used to identify lunar silicates (Greenhagen et al. 2010). Following the Christiansen feature, there is a steep drop-off in  $k$  and rise in  $n$ , causing a drop-off in emission followed by Reststrahlen features. For pyroxenes, spectral features in the  $\sim 8$ –22  $\mu\text{m}$  ( $\sim 1250$ –450  $\text{cm}^{-1}$ ) range are mainly due to Si-O stretching, Si-O-Si bending, and modes of the cation- $\text{O}_6$  octahedra. The positions of absorptions at these wavelengths vary with Mg# [defined as  $\text{Mg}/(\text{Mg} + \text{Fe})$ ] (Jäger et al. 1998; Hamilton 2000; Bowey et al. 2007; Klima et al. 2011b), likely due to the effect of the substitution on the octahedral layer, which in turn alters the Si-O vibrations (Hamilton 2000; Klima et al. 2007). To demonstrate these effects, Figure 18 shows the reflectance and optical constants for olivine (from Zeidler et al. 2011) ranging from the UV through the MIR, with the major spectroscopic features labeled. This figure also demonstrates that  $n$  and  $k$  values of silicates vary considerably in the mid-IR as compared with other wavelengths.

Amorphous pyroxenes produced by vapor phase condensation and synthetic glasses of pyroxene composition will lack many of the spectroscopic features of a crystalline pyroxene. As a result, the optical constants of these materials will have broader and fewer peaks than crystalline pyroxene. To date, little work has been done on oriented crystalline samples (Jäger

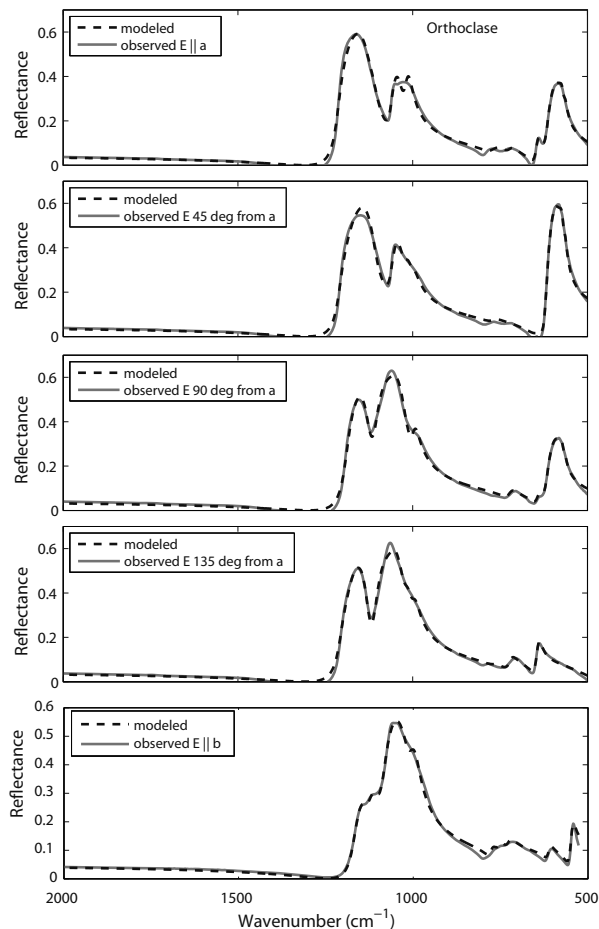


**FIGURE 15.** Measured and modeled reflectance spectra of orthoclase (Orth1) with incident E-field polarization parallel to  $a$ - $c$  plane at different polarization angles  $\phi$  (top four) and parallel to  $b$  (bottom).

et al. 1998), and none has been done to date on clinopyroxene. Figure 19 demonstrates the difference between optical constants of crystalline vs. amorphous phases. Additionally, oriented single-crystal spectra are preferable to orientation-averaged data acquired from pellets pressed from powders, as the lower maxima of the specular reflectance peaks of pellets results in lower maxima of derived optical constants when compared to orientation-averaged single-crystal optical constants (Roush et al. 1991).

## IMPLICATIONS

Radiative transfer models of planetary surfaces require optical constants for each component that may be present. Applying these models is difficult in the MIR due to the absence of optical constants for many important minerals in the monoclinic and triclinic crystal systems. We have applied the Berreman  $4 \times 4$  matrix method to derive the MIR optical constants of five different pyroxenes for which oriented single-crystal data were not previously reported in the literature. Four spectra with a polarized incident beam at different orientations were acquired for each sample, resulting in three sets of optical constants that can be used

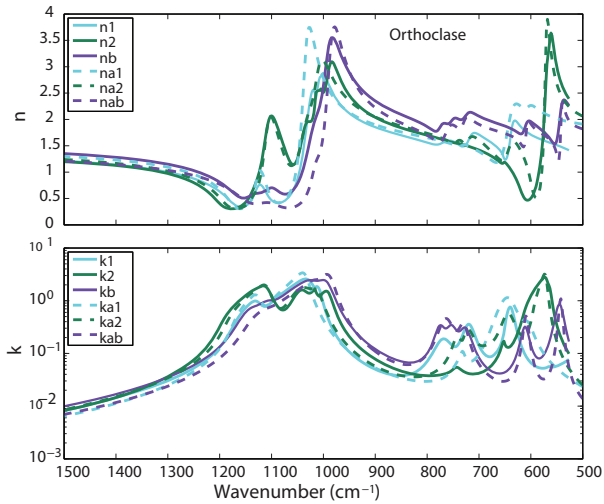


**FIGURE 16.** Optical constants ( $n$ ,  $k$ ) of orthoclase (Orth1) calculated in this work are in the solid lines ( $n1, k1, n2, k2, nb, kb$ ), while the optical constants derived in Aronson (1986) are in the dashed lines ( $na1, ka1, na2, ka2, nab, kab$ ). (Color online.)

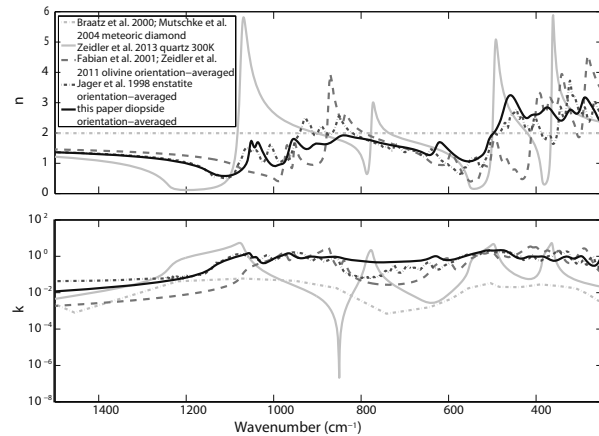


**FIGURE 17.** Orientation-averaged optical constants in the MIR for several minerals that belong to various crystal systems. Nano-diamonds from a Murchison meteorite (cubic), quartz (hexagonal), olivine (orthorhombic), and diopside (monoclinic).

to estimate  $n$  and  $k$  for a randomly oriented powdered sample. These data are necessary to improve compositional estimates of planetary regolith based on radiative transfer models.

The data presented here, in conjunction with a coupled optical-thermal model, such as that of Milan et al. (2011), can be used to model MIR emissivity spectra in a vacuum environment relevant to airless Solar System bodies. Modeled emission spectra can be compared to emissivity of the lunar surface derived from Diviner Lunar Radiometer data. These optical constants are also applicable to any MIR data from Mars or any airless Solar System objects including: existing spectra of asteroids from ISO, Spitzer, and any future data from James Webb Space Telescope (JWST) or the OSIRIS-REX mission. Future work will include

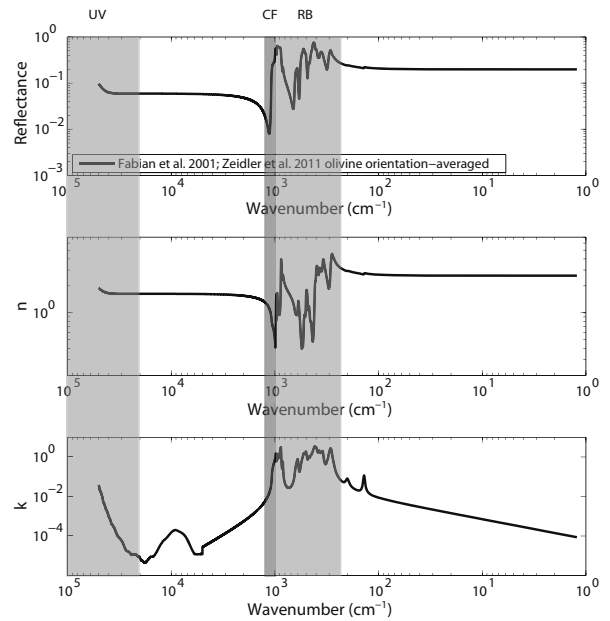


**FIGURE 18.** Orientation-averaged optical constants ( $n$ ,  $k$ ) of high-Mg olivine ( $Mg_{1.9}Fe_{0.1}SiO_4$ ) from UV to FIR wavelengths (Zeidler et al. 2011). Reflectance spectrum calculated from  $n$ ,  $k$  values. Labels: Christiansen feature (CF), Reststrahlen bands (RB), highlighted in gray.

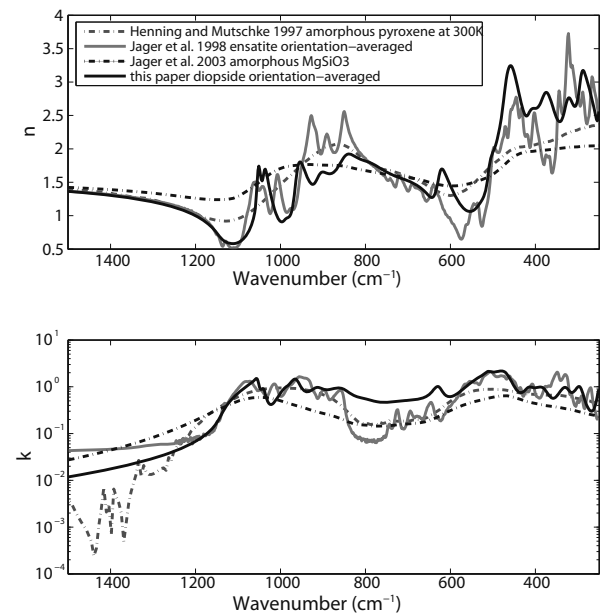


**FIGURE 19.** A comparison of single-crystal (enstatite and diopside) vs. amorphous (enstatite and a glass of pyroxene composition) pyroxene optical constants.

expanding the current version of the code to include the triclinic case. This code for triclinic minerals will be applied to obtain feldspar optical constants. The Matlab scripts developed for this work will be made publicly available to other researchers at <http://aram.ess.sunysb.edu/tglotch/>.

## ACKNOWLEDGMENTS

We thank D. Lindsley for providing two of the samples used in this work. This work was supported by NSF award no. AST-1150652 made to T.D.G. XRD analysis including face-indexation was supported by the U.S. Department of Energy, Office of Science, Office of Basic Energy Science, under contract DE-FG02-09ER46650. Diffraction data were collected on Stony Brook University Single-Crystal Diffractometer, obtained through the support of NSF (CHE-0840483).

## REFERENCES CITED

- Allen, C.C., Greenhagen, B.T., Donaldson Hanna, K.L., and Paige, D.A. (2011) Analysis of lunar pyroclastic deposit FeO abundances by LRO Diviner. *Journal of Geophysical Research: Planets*, 117, E00H28.
- Arnold, J.A., Glotch, T.D., Greenhagen, B.T., Thomas, I.R., and Bowles, N.E. (2013) Enhanced compositional analysis of the Moon using Diviner's long wavelength channels. *European Planetary Science Conference*, abstract 686.
- Aronson, J.R. (1986) Optical constants of monoclinic anisotropic crystals: Orthoclase. *Spectrochimica Acta Part A: Molecular Spectroscopy*, 42, 2-3, 187-190.
- Aronson, J.R., Emslie, A.G., Mises, E.V., Smith, E.M., and Strong, P.F. (1983) Optical constants of monoclinic anisotropic crystals: Gypsum. *Applied Optics*, 22, 24, 4093-4098.
- Aronson, J.R., Emslie, A.G., and Strong, P.F. (1985) Optical constants of triclinic anisotropic crystals: blue vitriol. *Applied Optics*, 24, 8, 1200-1203.
- Bandfield, J.L., Hamilton, V.E., and Christensen, P.R. (2000) A global view of martian surface compositions from MGS-TES. *Science*, 287, 5458, 1626-1630.
- Beintema, D.A. (1997) PAH's and crystalline silicates in planetary nebula. *Astrophysics and Space Science*, 225, 1-2, 507-512.
- Belousov, M.V., and Pavinich, V.F. (1978) Infrared reflection spectra of monoclinic crystals. *Optics and Spectroscopy*, 45, 5, 771-774.
- Bereman, D.W. (1972) Optics in stratified and anisotropic media: 4 × 4-matrix formulation. *Journal of the Optical Society of America*, 62, 4, 502-510.
- Born, M., and Wolf, E. (1999) *Principles of Optics*, p. 840. Cambridge University Press, U.K.
- Bouwman, J., Meeus, G., de Koter, A., Hony, S., Dominik, C., and Waters, L.B.F.M. (2001) Processing of silicate dust grains in Herbig Ae/Be systems. *Astronomy and Astrophysics*, 375, 950-962.
- Bowey, J.E., Morlock, A., Kohler, M., and Grady, M. (2007) 2-16 μm spectroscopy of micron-sized enstatite (Mg,Fe)<sub>2</sub>Si<sub>2</sub>O<sub>6</sub> silicates from primitive chondritic meteorites. *Monthly Notices of the Royal Astronomical Society*, 376, 3, 1367-1374.
- Braatz, A., Ott, U., Henning, Th., Jäger, C., and Jeschke, G. (2000) Infrared, ultraviolet, and electron paramagnetic resonance measurements on presolar diamonds: Implications for optical features and origin. *Meteoritics and Planetary Science*, 35, 1, 75-84.
- Bradley, J.P., Brownlee, D.E., and Veblen, D.R. (1983) Pyroxene whiskers and platelets in interplanetary dust - Evidence of vapour phase growth. *Nature*, 301, 473-477.
- Chapman, C.R., Morrison, D., and Zellner, B. (1975) Surface properties of asteroids: A synthesis of polarimetry, radiometry, and spectrophotometry. *Icarus*, 25, 1, 104-130.
- Conel, J.E. (1969) Infrared emissivities of silicates: Experimental results and a cloudy atmosphere model of spectral emission from condensed particulate mediums. *Journal of Geophysical Research*, 74, 6, 1614-1634.
- De Sanctis, M.C., Ammannito, E., Capria, M.T., Tosi, F., Capaccioni, F., Zambon, F., Carraro, F., Fonte, S., Frigeri, A., Jaumann, R., Magni, G., Marchi, S., McCord, T.B., McFadden, L.A., McSween, H.Y., Mittlefehldt, D.W., Nathues, A., Palomba, E., Pieters, C.M., Raymond, C.A., Russell, C.T., Toplis, M.J., and Turrini, D. (2012) Spectroscopic characterization of mineralogy and its diversity across Vesta. *Science*, 336, 6082, 697-700.
- Donaldson Hanna, K.L., Thomas, I.R., Bowles, N.E., Greenhagen, B.T., Pieters, C.M., Mustard, J.F., Jackson, C.R.M., and Wyatt, M.B. (2012) Laboratory emissivity measurements of the plagioclase solid solution series under varying environmental conditions. *Journal of Geophysical Research*, 117, E11004, 7pp.
- Dorschner, J., Begemann, B., Henning, T., Jaeger, C., and Mutschke, H. (1995) Steps toward interstellar silicate mineralogy. II. Study of Mg-Fe-silicate glasses of variable composition. *Astronomy and Astrophysics*, 300, 503-520.
- Dyar, M.D., Sklute, E.C., Menzies, O.N., Bland, P.A., Lindsley, D., Glotch, T., Lane, M.D., Schaefer, M.W., Wopenka, B., Klima, R., Bishop, J.L., Hiroi, T., Pieters, C., and Sunshine, J. (2009) Spectroscopic characteristics of synthetic olivine: An integrated multi-wavelength and multi-technique approach. *American Mineralogist*, 94, 7, 883-898.
- Fabian, D., Henning, T., Jäger, C., Mutschke, H., Dorschner, J., and Wehrhan, O. (2001) Steps toward interstellar silicate mineralogy. *Astronomy and Astrophysics*, 378, 1, 228-238.
- Glotch, T.D., and Rogers, A.D. (2013) Evidence for magma-carbonate interaction beneath Syrtis Major, Mars. *Journal of Geophysical Research: Planets*, 118, 126-137.
- Glotch, T.D., and Rossman, G.R. (2009) Mid-infrared reflectance spectra and optical constants of six iron oxide/oxyhydroxide phases. *Icarus*, 204, 2, 663-671.
- Glotch, T.D., Christensen, P.R., and Sharp, T.G. (2006) Fresnel modeling of hematite crystal surfaces and application to martian hematite spherules. *Icarus*, 181, 408-418.
- Glotch, T.D., Rossman, G.R., and Aharonson, O. (2007) Mid-infrared (5-100 μm) reflectance spectra and optical constants of 10 phyllosilicate minerals. *Icarus*, 192, 605-662.
- Glotch, T.D., Lucey, P.G., Bandfield, J.L., Greenhagen, B.T., Thomas, I.R., Elphic, R.C., Bowles, N.E., Wyatt, M.B., Allen, C.C., Donaldson Hanna, K.L., and Paige, D.A. (2010) Highly silicic compositions on the Moon. *Science*, 329, 5998, 1510-1513.
- Glotch, T.D., Hagerty, J.J., Lucey, P.G., Hawke, B.R., Giguere, T.A., Arnold, J.A., Williams, J.-P., Jolliff, B.L., and Paige, D.A. (2011) The Mairan Domes: Silicic volcanic constructs on the Moon. *Geophysical Research Letters*, 38, L21204, <http://dx.doi.org/10.1029/2011GL049548>.
- Greenhagen, B.T., Lucey, P.G., Wyatt, M.B., Glotch, T.D., Allen, C.C., Arnold, J.A., Bandfield, J.L., Bowles, N.E., Hanna, K.L.D., Hayne, P.O., Song, E., Thomas, I.R., and Paige, D.A. (2010) Global silicate mineralogy of the Moon from the Diviner Lunar Radiometer. *Science*, 329, 5998, 1507-1509.
- Griffiths, D.J. (1999) *Introduction to Electrodynamics*, 3rd ed., 576 p. Prentice Hall, Upper Saddle River, New Jersey.
- Hamilton, V.E. (2000) Thermal infrared emission spectroscopy of the pyroxene mineral series. *Journal of Geophysical Research*, 105, E, 4, 9701-9716.
- Hamilton, V.E., Christensen, P.R., McSween, H.Y., and Bandfield, J.L. (2001) Searching for the source regions of martian meteorites using MGS TES: Integrating martian meteorites into the global distribution of igneous materials on Mars. *Meteoritics and Planetary Science*, 38, 6, 871-885.
- Hamner, M.S., Lynch, D.K., and Russel, R.W. (1994) The 8-13 micron spectra of comets and the composition of silicate grains. *Astrophysical Journal, Part I*, 425, 1, 274-285.
- Hapke, B. (1993) *Theory of Reflectance and Emittance Spectroscopy*, 472 p. Cambridge University Press, U.K.
- (2012) *Theory of Reflectance and Emittance Spectroscopy*, 2nd edition, 528 p. Cambridge University Press, U.K.
- Henning, T., and Mutschke, H. (1997) Low-temperature infrared properties of cosmic dust analogs. *Astronomy and Astrophysics*, 327, 743-754.
- Ivanovski, V., Mayerhöfer, T.G., and Popp, J. (2007) Isobestic-like point in the polarized reflectance spectra of monoclinic crystals—A quantitative approach. *Spectrochimica Acta Part A: Molecular and Biomolecular Spectroscopy*, 68, 3, 632-638.
- Jäger, C., Molster, F.J., Dorschner, J., Henning, Th., Mutschke, H., and Waters, L.B.F.M. (1994) Steps toward interstellar silicate mineralogy. IV. The crystalline revolution. *Astronomy and Astrophysics*, 339, 904-916.
- Jäger, C., Mutschke, H., Begemann, B., Dorschner, J., and Henning, T. (1998) Steps toward interstellar silicate mineralogy. I: Laboratory results of a silicate glass of mean cosmic composition. *Astronomy and Astrophysics*, 292, 2, 641-655.
- Jäger, C., Dorschner, J., Mutschke, H., Posch, T., and Henning, T. (2003) Steps toward interstellar silicate mineralogy. VII. Spectral properties and crystallization behaviour of magnesium silicates produced by the sol-gel method. *Astronomy and Astrophysics*, 408, 193-204.
- Johnson, E.A., Rossman, G.R., Dyar, M.D., and Valley, J.W. (2002) Correlation between OH concentration and oxygen isotope diffusion rate in diopside from the Adirondack Mountains, New York. *American Mineralogist*, 87, 7, 899-908.
- Karner, J., Papike, J.J., and Shearer, C.K. (2006) Comparative planetary mineralogy: Pyroxene major- and minor-element chemistry and partitioning of vanadium between pyroxene and melt in planetary basalts. *American Mineralogist*, 91, 10, 1574-1582.
- Klima, R.L., Pieters, C.M., and Dyar, M.D. (2007) Spectroscopy of synthetic Mg-Fe pyroxenes I: Spin-allowed and spin-forbidden crystal field bands in the visible and near-infrared. *Meteoritics and Planetary Science*, 42, 2, 235-253.
- (2008) Characterization of the 1.2 μm M1 pyroxene band: Extracting cooling history from near-IR spectra of pyroxenes and pyroxene-dominated rocks. *Meteoritics and Planetary Science*, 43, 10, 1591-1604.
- Klima, R.L., Pieters, C.M., Boardman, J.W., Green, R.O., Head, J.W. III, Isaacson, P.J., Mustard, J.F., Nettles, J.W., Petro, N.E., Staid, M.I., Sunshine, J.M., Taylor, L.A., and Tompkins, S. (2011a) New insights into lunar petrology: Distribution and composition of prominent low-Ca pyroxene exposures as observed by the Moon Mineralogy Mapper (M<sup>3</sup>). *Journal of Geophysical Research*, 116, E00G06.
- Klima, R.L., Dyar, M., and Pieters, C.M. (2011b) Near-infrared spectra of clinopyroxenes: Effects of calcium content and crystal structure. *Meteoritics & Planetary Science*, 46, 379-395.
- Lane, M.D. (1999) Midinfrared optical constants of calcite and their relationship to particle size effects in thermal emission spectra of granular calcite. *Journal of Geophysical Research: Planets*, 104, 14099-14108.
- Liu, D. (2012) An improved radiative transfer model for estimating mineral abundance of immature and mature lunar soils. 43rd Lunar and Planetary Science Conference, 1659.
- Logan, L.M., Hunt, G.R., Salisbury, J.W., and Balsamo, S.R. (1973) Compositional implications of Christiansen frequency maximums for infrared remote sensing

- applications. *Journal of Geophysical Research*, 78, 23, 4983–5003.
- Long, L.L., Querry, M.R., Bell, R.J., and Alexander, R.W. (1992) Optical properties of calcite and gypsum in crystalline and powdered form in the infrared and far-infrared. *Infrared Physics*, 34, 2, 191–201.
- Lucy, P.G. (1998) Model near-infrared optical constants of olivine and pyroxene as a function of iron content. *Journal of Geophysical Research: Planets*, 103, E, 1, 1703–1713.
- Lumme, K., and Bowell, E. (1981) Radiative transfer in the surfaces of atmosphereless bodies. I. Theory. *The Astronomical Journal*, 86, 11, 1694–1721.
- Mackinnon, I.D.R., and Rietmeijer, F.J.M. (1987) Mineralogy of chondritic interplanetary dust particles. *Review of Geophysics*, 25, 7, 1527–1553.
- Mayerhöfer, T.G., and Popp, J. (2007) Employing spectra of polycrystalline materials for the verification of optical constants obtained from corresponding low-symmetry single crystals. *Applied Optics*, 46, 3, 327–334.
- Mayerhöfer, T.G., Weber, S., and Popp, J. (2010) Simplified formulas for non-normal reflection from monoclinic crystals. *Optics Communications*, 284, 3, 719–723.
- McCord, T.B., Adams, J.B., and Johnson, T.V. (1970) Asteroid Vesta: Spectral reflectivity and compositional implications. *Science*, 168, 3938, 1445–1447.
- Milan, L., Thomas, I., and Bowles, N. (2011) Lunar regolith thermal gradients and emission spectra: Modeling and validation. *Journal of Geophysical Research*, 116, E12003.
- Mishchenko, M.I., Dlugach, J.M., Yanovitskij, E.G., and Zakharova, N.T. (1999) Bidirectional reflectance of flat, optically thick particulate layers; an efficient radiative transfer solution and applications to snow and soil surfaces. *Journal of Quantitative Spectroscopy and Radiative Transfer*, 63, 2–6, 409–432.
- Molster, F., and Kemper, C. (2004) Crystalline silicates. *Space Science Reviews*, 119, 1–4, 3–28.
- Molster, F.J., Waters, L.B.F.M., Tielens, A.G.G.M., and Barlow, M.J. (2002) Crystalline silicate dust around evolved stars. *Astronomy and Astrophysics*, 382, 184–221.
- Mutschke, H., Andersen, A.C., Jäger, C., Henning, T., and Braatz, A. (2004) Optical data of meteoritic nano-diamonds from far-ultraviolet to far-infrared wavelengths. *Astronomy and Astrophysics*, 423, 983–993.
- Ody, A., Poulet, F., Langevin, Y., Bibring, J.P., Bellucci, G., Altieri, F., Gondet, B., Vincendon, M., Carter, J., and Manaud, N. (2012) Global maps of anhydrous minerals at the surface of Mars from OMEGA/MEx. *Journal of Geophysical Research: Planets*, 117, E00J14.
- Paige, D.A., Foote, M.C., Greenhagen, B.T., Schofield, J.T., Calcutt, S., Vasavada, A.R., Preston, D.J., Taylor, F.W., Allen, C.C., Snook, K.J., Jakosky, B.M., Murray, B.C., Soderblom, L.A., Jau, B., Loring, S., Bulharowski, J., Bowles, N.E., Thomas, I.R., Sullivan, M.T., Avis, C., Jong, E.M., Hartford, W., and McCleese, D.J. (2010) The Lunar reconnaissance orbiter diviner lunar radiometer experiment. *Space Science Reviews*, 150, 1–4, 125–160.
- Pavinich, V.F., and Belousov, M.V. (1978) Dispersion analysis of reflection spectra of monoclinic crystals. *Optics and Spectroscopy* 45, 881. (Translated from *Opt. Spektrosk.*, 45, 1114.)
- Ramsey, M.S., and Christensen, P.R. (1998) Mineral abundance determination: Quantitative deconvolution of thermal emission spectra. *Journal of Geophysical Research*, 103, B, 1, 577–596.
- Rogers, A.D., and Christensen, P.R. (2007) Surface mineralogy of Martian low-albedo regions from MGS-TES data: Implications for upper crustal evolution and surface alteration. *Journal of Geophysical Research*, 112, E01003.
- Rogers, A.D., Bandfield, J.L., and Christensen, P.R. (2007) Global spectral classification of Martian low-albedo regions with Mars Global Surveyor Thermal Emission Spectrometer (MGS-TES) data. *Journal of Geophysical Research*, 112, E02004.
- Roush, T., Pollack, J., and Orenberg, J. (1991) Derivation of midinfrared (5–25  $\mu\text{m}$ ) optical constants of some silicates and palagonite. *Icarus*, 94, 1, 191–208.
- Salisbury, J.W. (1972) Spectroscopic remote sensing of lunar surface composition. *Earth, Moon and Planets*, 5, 3–3, 332–347.
- Salisbury, J.W., and Walter, L.S. (1989) Thermal infrared (2.5–13.5  $\mu\text{m}$ ) spectroscopic remote sensing of igneous rock types on particulate planetary surfaces. *Journal of Geophysical Research: Solid Earth*, 94, B7, 9192–9202.
- Seitz, F. (1940) *Modern Theory of Solids*. McGraw-Hill, New York.
- Shkuratov, Y., Starukhina, L., Hoffman, H., and Arnold, G. (1999) A model of spectral albedo of particulate surfaces: Implications for optical properties of the moon. *Icarus*, 137, 2, 235–246.
- Shkuratov, Y.G., Kaydash, V.G., and Pieters, C.M. (2004) Lunar clinopyroxene and plagioclase: Surface distribution and composition. *Solar System Research*, 39, 4, 255–266. [Translated from *Astronomicheskii Vestnik*, 39, 4, 2005, 291–303 (in Russian).]
- Song, E., Bandfield, J.L., Lucey, P.G., Greenhagen, B.T., and Paige, D.A. (2013) Bulk mineralogy of lunar crater central peaks via thermal infrared spectra from the Diviner Lunar Radiometer: A study of the Moon's crustal composition at depth. *Journal of Geophysical Research: Planets*, 118, 4, 689–707.
- Sogawa, H., Koike, C., Chihara, H., Suto, H., Tachibana, S., Tsuchiyama, A., and Kozasa, T. (2006) Infrared reflection spectra of forsterite crystal. *Astronomy and Astrophysics*, 451, 357–361.
- Spitzer, W.G., and Kleinman, D.A. (1961) Infrared lattice bands of quartz. *Physical Review*, 121, 5, 1324–1335.
- Spitzer, W.G., Kleinman, D.A., and Walsh, D. (1959) Infrared properties of hexagonal silicon carbide. *Physical Review*, 113, 1, 127–132.
- Sunshine, J.M., Bus, J., McCoy, T.J., Burbine, T.H., Corrigan, C.M., and Binzel, R.P. (2004) High-calcium pyroxene as an indicator of igneous differentiation in asteroids and meteorites. *Meteoritics and Planetary Science*, 39, 8, 1343–1357.
- Suto, H., Koike, C., Sogawa, H., Tsuchiyama, A., Chihara, H., and Mizutani, K. (2002) Infrared spectra of fayalite crystal. *Astronomy and Astrophysics*, 389, 568–571.
- Tompkins, S., and Pieters, C.M. (1999) Mineralogy of the lunar crust: Results from Clementine. *Meteoritics and Planetary Science*, 34, 25–41.
- Wenrich, M.L., and Christensen, P.R. (1996) Optical constants of minerals derived from emission spectroscopy: Application to quartz. *Journal of Geophysical Research: Solid Earth*, 101, 15921–15931.
- Yeh, P. (1979) Optics of anisotropic layered media: A new  $4 \times 4$  matrix algebra. *Surface Science*, 96, 1–3, 41–53.
- Zeidler, S., Posch, T., Mutschke, H., Richter, H., and Wehrhan, O. (2011) Near-infrared absorption properties of oxygen-rich stardust analogs. The influence of coloring metal ions. *Astronomy and Astrophysics*, 526, 68.
- Zeidler, S., Posch, T., and Mutschke, H. (2013) Optical constants of refractory oxides at high temperatures. Mid-infrared properties of corundum, spinel, and alpha-quartz, potential carriers of the 13  $\mu\text{m}$  feature. *Astronomy and Astrophysics*, 553, 81.

MANUSCRIPT RECEIVED DECEMBER 3, 2013

MANUSCRIPT ACCEPTED APRIL 24, 2014

MANUSCRIPT HANDLED BY BORIANA MIHALOVA